processes

MDPI

*Article*

# Evolution of Mechanical Parameters in Fractured Carbonate Rocks Under Simulated High-Stress Conditions of Ultra-Deep Reservoirs

**Zhimin Wang [1,2,3,4], Hui Zhang [1,2,3,4], Haoyang Zan [1,2], Xin Wang [1,2], Ziwei Liu [1,2], Wentao Zhang [1,2], Xiang Zhang [5,*], Changsheng Ma [5], Yaozheng Duan [5] and Wendong Yang [5,*]**

1 PetroChina Tarim Oilfield Company, Korla 841000, China
2 R&D Center for Ultra-Deep Complex Reservoir Exploration and Development, China National Petroleum Corporation, Korla 841000, China
3 Engineering Research Center for Ultra-Deep Complex Reservoir Exploration and Development, Xinjiang Uygur Autonomous Region, Korla 841000, China
4 Xinjiang Key Laboratory of Ultra-Deep Oil and Gas, Korla 841000, China
5 State Key Laboratory of Deep Oil and Gas, China University of Petroleum (East China), Qingdao 266580, China
* Correspondence: upc_zhangxiang@126.com (X.Z.); wendongy@gmail.com (W.Y.)

## Abstract

The ultra-deep carbonate reservoirs of the Fuman Oilfield in the Tarim Basin are characterized by intense fracture development. The coupled effects of high in-situ stress and fracture structures significantly deteriorate the mechanical properties of the rock mass, thereby constraining wellbore stability evaluation and safe drilling and completion operations. Existing studies have primarily focused on medium- to low-confining-pressure conditions and isolated fracture parameters, making it difficult to characterize the mechanical response of fractured rock masses under the high-stress conditions of ultra-deep reservoirs. To address this issue, limestone from the Yingshan Formation of the target reservoir was selected as the research object, and fractured specimens with varying fracture angles, widths, and densities were prepared. Uniaxial compression tests and triaxial compression tests under high confining pressures of 90 MPa and 120 MPa were conducted to systematically reveal the evolution of rock strength, deformation parameters, shear strength parameters, and failure modes under the coupled influence of fracture geometric parameters and confining pressure. On this basis, a confining-pressure–fracture coupled damage prediction model was established, and wellbore stability around the reservoir was analyzed using Finite Difference Method. The results indicate that fracture angle causes the peak strength and Young's modulus to first decrease and then increase, with an inclination angle near 45° representing the most unfavorable fracture orientation. Increases in fracture width and density lead to continuous degradation of strength and stiffness. Although high confining pressure can close fractures and enhance load-bearing capacity, it cannot eliminate the controlling influence of fractures on failure pathways. Sensitivity analysis shows that the Young's modulus and Poisson's ratio are most sensitive to fracture width; cohesion is mainly governed by fracture width and density; and the internal friction angle is most sensitive to fracture density. Numerical simulations of wellbore stability further confirm that medium-inclination, large-aperture, and high-density fractures significantly increase the risk of wellbore instability. The findings provide experimental and theoretical support for mechanical-parameter correction, wellbore stability assessment, and construction-risk control in ultra-deep fractured carbonate reservoirs.



Academic Editor: Dicho Stratiev

Received: 30 May 2026
Revised: 17 June 2026
Accepted: 24 June 2026
Published: 29 June 2026

**Keywords:** ultra-deep reservoirs; carbonate rocks; fractured rock mass; rock mechanics; mechanical parameter evolution; reservoir stability

## 1. Introduction

As China's deep-ultra-deep oil and gas exploration and development continue to advance in depth, the ultra-deep carbonate reservoirs in the Fuman Oilfield of the Tarim Basin have become an important position for increasing reserves and production [1], as shown in Figure 1.

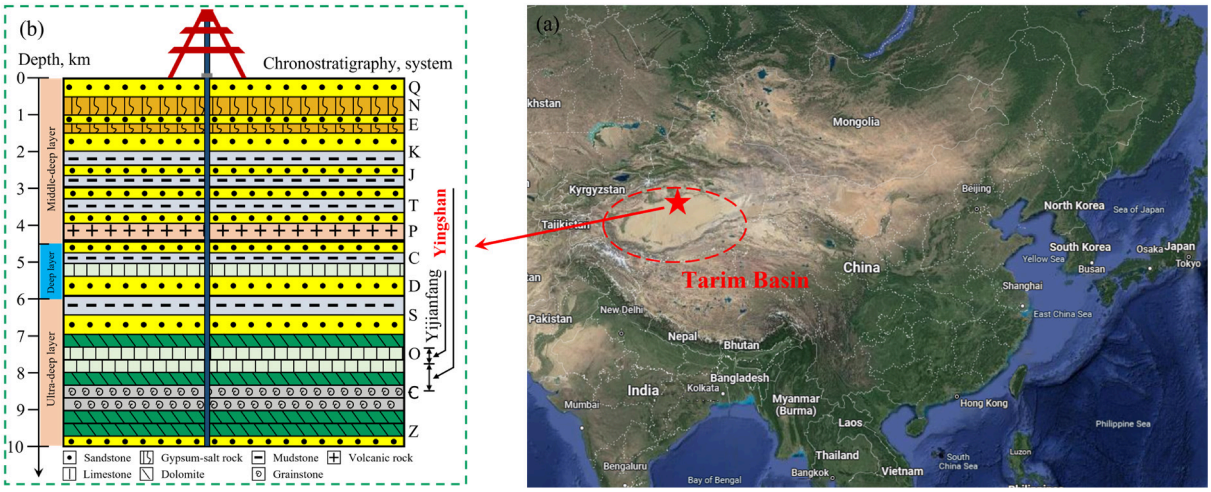


**Figure 1.** Geographical location of the Fuman Oilfield in the Tarim Basin and stratigraphic position of the Yingshan Formation. (**a**) Map of China and the location of the Tarim Basin; (**b**) location of the Yingshan Formation.

This type of reservoir has a large, buried depth (more than 7000 m), high in-situ stress level, and local formation confining pressure that can reach more than 90 MPa. At the same time, it is controlled by tectonic movement, diagenesis, and dissolution transformation. Natural fractures and fracture-cavity systems are widely developed [2,3]. The existence of fractures changes the internal stress transfer path and local damage evolution mode of rock mass, which makes the reservoir rock mass show significant heterogeneity, anisotropy, and strength discreteness. These characteristics directly affect the evaluation of wellbore stability, reservoir fracturing, injection-production parameter optimization, and construction risk control. Therefore, clarifying the evolution law of mechanical parameters and failure mechanism of fractured carbonate rocks under ultra-deep and high stress conditions is a key basic problem for the safe and efficient development of deep oil and gas engineering.

Focusing on the mechanical response of fractured rock mass, the existing studies have systematically revealed the control effect of fracture geometric characteristics on the strength, deformation, and fracture mode of rock mass from the fracture initiation, propagation, coalescence, and instability failure process of single fracture or multi-fracture specimens [4–7]. Further research shows that the fracture angle, opening, density, and spatial combination will significantly affect the fracture tip stress concentration, fracture propagation path, energy dissipation process, and post-peak failure mode [8–18]. In addition to experimental research, numerical methods, such as finite element, discrete element, finite-discrete element coupling, and particle flow are also widely used to simulate the progressive failure process of fractured rock mass from local damage to overall instability,

which provides important support for understanding the meso-fracture mechanism and macro-strength degradation law of fractured rock mass [19–23]. In general, the existing research has fully proved that the geometric parameters of fractures are the core factors controlling the degradation of mechanical properties of rock mass. However, most experiments are still focused on rock-like materials, sandstone, granite and other objects, and are mainly based on uniaxial or medium-low confining pressure conditions. The understanding of the influence of fracture parameters under high confining pressure environment in ultra-deep reservoirs is still insufficient.

With the increasing depth of engineering mining, the study of deep rock mechanics has gradually shifted from conventional loading conditions to extreme environments such as in-situ stress, high temperature, high water pressure, and complex stress paths. Related studies have shown that deep rocks will exhibit compaction, yield, dilatancy, brittle-ductile transformation, and energy release characteristics different from shallow rocks under high stress [24–28]. The tests of true triaxial loading, cyclic disturbance, high temperature-stress coupling, and hydraulic-mechanical coupling further reveal the sensitivity of deep rock mechanical behavior to confining pressure, ground temperature, pore pressure, and loading path [29–38]. For ultra-deep carbonate reservoirs, the existing research has carried out useful explorations from the aspects of exploration and development theory, reservoir geomechanics, rock physical characteristics, and triaxial compression behavior [39–43], and formed a relatively rich method system in dynamic mechanics, creep damage, and deep in-situ environment reconstruction [44–47]. These results show that high in-situ stress will not only improve the overall bearing capacity of rock mass, but also change the mechanism of fracture closure, slip, expansion, and penetration. Therefore, the law of fractured rock mass under shallow or medium-low confining pressure cannot be simply extrapolated to ultra-deep reservoirs.

The evolution of mechanical parameters is an important bridge between rock failure mechanism and engineering stability evaluation. A large number of experiments and numerical analysis have been carried out on the Young's modulus, Poisson's ratio, peak strength, cohesion, internal friction angle, and energy evolution law of rock mass with notch, joint, hole, or non-flat fracture [48–54]. At the same time, based on the constitutive model of damage mechanics, elastoplastic theory, and water-rock coupling theory, the progressive damage, strength degradation, and parameter degradation characteristics of fractured rock mass during loading are further described [55–57]. However, the existing results pay more attention to the influence of general fractured rock mass or single fracture parameters on mechanical properties, and there is a lack of systematic comparison of the differential effects of fracture angle, width, and density in high confining pressure environment. Especially for ultra-deep carbonate rocks, which are highly heterogeneous, highly fractured, and have extremely high engineering stress levels, how the deformation parameters, strength parameters, and failure modes evolve with the geometric characteristics of fractures still lacks a direct laboratory test basis.

In summary, the existing research has laid an important foundation for understanding the fracture mechanism of fractured rock mass and the mechanical behavior of deep rock. However, for the ultra-deep carbonate reservoir in the Fuman Oilfield of the Tarim Basin, there are still the following shortcomings. First, the existing fractured rock mass tests are mostly concentrated in medium and low confining pressure or uniaxial conditions, which is difficult to reflect the coupling effect of fracture closure, slip, and expansion under high geo-stress environment above 90 MPa. Secondly, most of the existing studies focus on the single factor such as fracture dip angle, and lack of understanding of the strength degradation law under the joint action of fracture width, density, and confining pressure. Thirdly, there is still a lack of systematic quantitative analysis of engineering reservoir

conditions for the internal relationship between elastic parameters, strength parameters, and failure modes of fractured carbonate rocks.

Based on this, this paper takes the carbonate rocks of Yingshan Formation in Fuman Oilfield of Tarim Basin as the research object, prepares fractured rock mass specimens with different fracture angles, widths, and densities, and carries out uniaxial and triaxial compression tests under confining pressures of 0 MPa, 90 MPa, and 120 MPa. The evolution laws of stress–strain response, elastic parameters, strength parameters, and failure modes of rock mass under the combined action of fracture geometric parameters and high confining pressure are systematically analyzed. The research results can provide experimental basis for rock mechanics parameter evaluation and construction risk control of ultra-deep carbonate reservoirs.

## 2. Experimental Preparation and Methods

### 2.1. Specimen Preparation

The experimental research object of this paper is carbonate rock, which is selected from Fuman Oilfield in Tarim Basin. It belongs to Yingshan Formation, and the lithology is mainly thick gray limestone [58]. According to the Standard for Experiment Methods for Engineering Rock Masses (GB/T 50266-2013 [59]), the rock was processed into a cylinder specimen of $\phi$ 25 $\times$ $h$ 50 mm. In order to study the influence of fracture conditions on the mechanical properties of rock, the specimens were cut from the middle, and the fractures with different angles, widths, and densities were prefabricated on the section. The angles were 0°, 30°, 45°, 60°, and 90° respectively based on the horizontal direction. The first group in the width was the blank control group, and the fracture widths were 2 mm, 4 mm, 6 mm, and 8 mm, respectively. The density was measured by the number of strips in the specimen section, and 2, 4, 6, 8, and 10 strips were set, respectively.

Natural reservoir fractures commonly exhibit surface roughness, nonuniform aperture, local mineral infilling, and complex contact morphologies, all of which can significantly influence the frictional resistance, interlocking effect, and shear-slip behavior of fracture surfaces. Considering that this study focuses on the independent effects of three geometric parameters—fracture inclination angle, fracture width, and fracture density—simplified smooth prefabricated fracture surfaces were adopted in the experiments to avoid introducing substantial randomness from additional factors such as fracture roughness, infilling materials, and nonuniform aperture. This treatment facilitates the identification, under controlled conditions, of the influence of different fracture geometric parameters on mechanical properties such as peak strength, Young's modulus, Poisson's ratio, cohesion, and internal friction angle.

The effect of fracture prefabrication is shown in Figure 2b, and the prefabricated specimen is shown in Figure 2c. After fracture preparation, the two cut portions of each specimen were aligned along the original cutting plane and reassembled to restore the overall cylindrical geometry. During reassembly, a heat-shrink sleeve was used to constrain the specimen, ensuring coaxial alignment of the two parts and minimizing the influence of eccentric loading. No adhesive was used in this study; instead, contact between the two parts of the specimen was maintained primarily by the external constraint and the subsequent confining pressure. For specimens subjected to triaxial compression tests, the outer surface was further wrapped with a heat-shrink sleeve before loading to prevent silicone oil from entering the internal fractures. All specimens with prefabricated fractures were placed in a dry environment for two weeks prior to testing to reduce the influence of differences in internal moisture conditions on the experimental results.

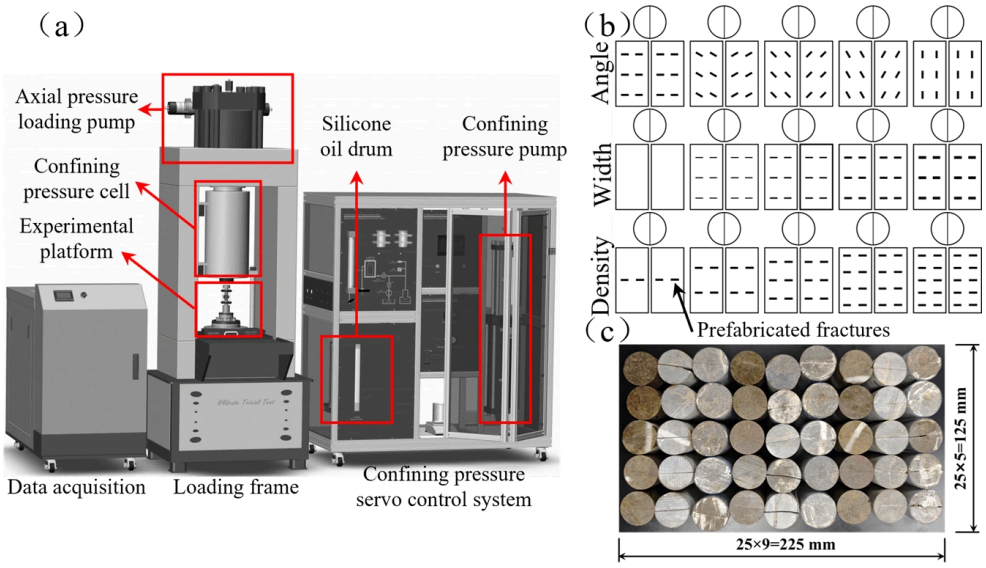


**Figure 2.** Carbonate rock specimens and experimental apparatus. (**a**) Multi-field coupling rock triaxial test system; (**b**) schematic diagram or preparation pattern of prefabricated fractures; (**c**) prefabricated fractured carbonate rock specimens.

The density of the specimen is between 2.520–2.707 g/cm$^3$, and the average density is 2.610 g/cm$^3$. Before the experiment, the prefabricated specimen was placed in a dry place for two weeks to eliminate the influence of internal water content.

Because natural carbonate rocks exhibit pronounced heterogeneity, differences may exist among specimens in mineral composition, grain structure, microfracture development, pores, and local calcite veins. These natural variations may lead to a certain degree of discreteness in specimen strength, deformation modulus, and failure mode. To minimize this influence as much as possible, cores with similar lithology, relatively intact structures, and fewer visible defects were preferentially selected for specimen preparation in this study. The mineral composition of the specimens was analyzed by X-ray diffraction (XRD). The results of mineral composition analysis are shown in Figure 3. It can be seen from Figure 3a that the mineral composition of the selected specimens mainly includes calcite, dolomite, quartz, and clay minerals. It can be seen from Figure 3b that the content of calcite is the highest, the content of dolomite is the second, and the content of quartz and clay minerals is less. The average contents of calcite, dolomite, quartz, and clay minerals are 82.86%, 8.69%, 5.48%, and 2.97%, respectively.

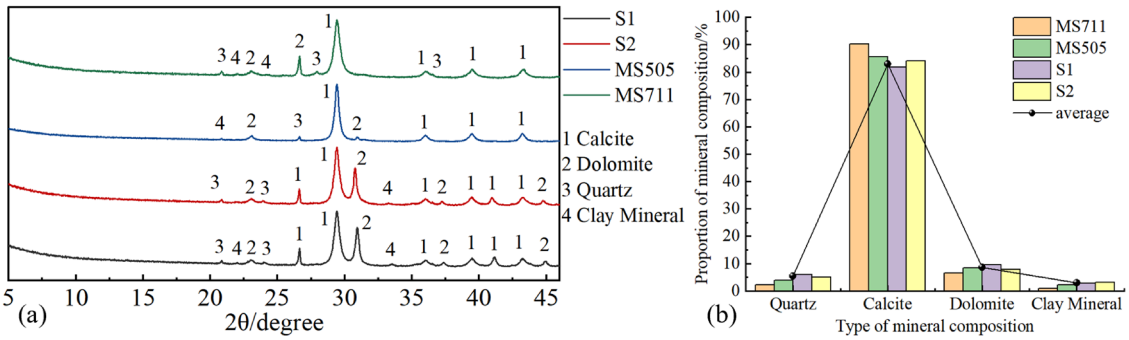


**Figure 3.** Mineralogical composition analysis of carbonate rock specimens. (**a**) XRD patterns of different specimens, where 1, 2, 3, and 4 represent calcite, dolomite, quartz, and clay minerals, respectively; (**b**) mineral contents of different specimens and their average values.

The above results indicate that the specimens exhibit a certain degree of lithological consistency; however, data discreteness caused by the inherent heterogeneity of natural rocks cannot be completely eliminated. Therefore, in interpreting the experimental results, this study places greater emphasis on the relative variation trends of mechanical parameters under different fracture inclination angles, widths, and densities, rather than directly regarding the measured value of a single specimen as a representative parameter of the natural reservoir rock mass.

### 2.2. Experiment Scheme

The multi-field coupling rock triaxial test system was used to carry out the experiment (Figure 2a). The maximum axial pressure of the experiment system is 1500 kN and the maximum confining pressure is 200 MPa.

In order to explore the mechanical properties of fractured rocks under ultra-deep in-situ stress environment, rock mechanics experiments under confining pressure of 0 MPa, 90 MPa, and 120 MPa were carried out, respectively. The orthogonal experimental design is shown in Table 1. Considering the great difficulty of obtaining ultra-deep carbonate rock cores, as well as the high requirements of high-confining-pressure triaxial compression tests for specimen integrity, machining accuracy, and testing-system stability, only one specimen was prepared for each combination of fracture parameters. Therefore, the results of this study are mainly used for comparative analysis of the variation trends in mechanical responses under different fracture geometries, rather than being regarded as universally applicable parameters in a strict statistical sense.

**Table 1.** Experimental scheme for fractured rock mass.

| Confining Pressure Condition/MPa | Fracture Parameters | | |
|---|---|---|---|
| | Angle/° | Width/mm | Density/Strip |
| 0, 90, 120 | 0, 30, 45, 60, 90 | 0, 2, 4, 6, 8 | 2, 4, 6, 8, 10 |

The Young's modulus and Poisson's ratio of fractured rock mass are calculated according to the pre-peak elastic section of stress–strain curve, and the calculation equations are as follows: Equations (1) and (2).

$$E = \frac{\Delta\sigma}{\Delta\varepsilon} \tag{1}$$

$$\mu = -\frac{\Delta\varepsilon_3}{\Delta\varepsilon_1} \tag{2}$$

In the equation, $E$ is the Young's modulus; $\Delta\sigma$ is the difference between the end stress and the initial stress of the elastic section of the stress-strain curve; $\Delta\varepsilon$ is the difference between the end-point axial strain and the initial axial strain of the elastic section of the stress-strain curve; $\mu$ is Poisson's ratio; $\varepsilon_1$ is axial strain; $\varepsilon_3$ is radial strain; $\Delta\varepsilon_1$ is the difference between the end-point axial strain and the initial axial strain of the elastic section of the stress-strain curve; $\Delta\varepsilon_3$ is the difference between the end-point radial strain and the initial radial strain of the elastic section of the stress-strain curve.

According to Equation (3), the sensitivity of mechanical parameters and strength parameters of fractured rock mass to different fractures is calculated:

$$S_X = \left| \frac{\Delta P / P_0}{\Delta X / X_0} \right| \tag{3}$$

In the equation, $S_X$ is the sensitivity coefficient of fracture parameter $X$ to mechanical parameter $P$; $P_0$ is the benchmark mechanical parameter; $\Delta P$ is the variation of me-

chanical parameters; $X_0$ is the benchmark fracture parameter; $\Delta X$ is the variation of fracture parameters.

## 3. Experiment Results and Analysis

### *3.1. Stress–Strain Response Characteristics of Fractured Rock Mass*

Axial cutting and subsequent reassembly may exert a certain influence on the local contact state of the specimens. To examine the effect of this treatment on the overall load-bearing capacity of the specimens, comparative tests were conducted on intact specimens and axially cut-and-reassembled specimens without internal prefabricated fractures, as shown in Figure 4. The results show that, in the absence of prefabricated fractures, the stress–strain responses and compressive strengths of the intact specimens and the axially cut-and-reassembled specimens differ only slightly under uniaxial conditions and confining pressures of 90 MPa and 120 MPa. This indicates that the axial cutting and reassembly process itself has a relatively limited effect on the basic compressive mechanical response of the specimens. Therefore, the subsequent differences in mechanical properties among the specimens can be primarily attributed to variations in the inclination angle, width, and density of the prefabricated fractures.

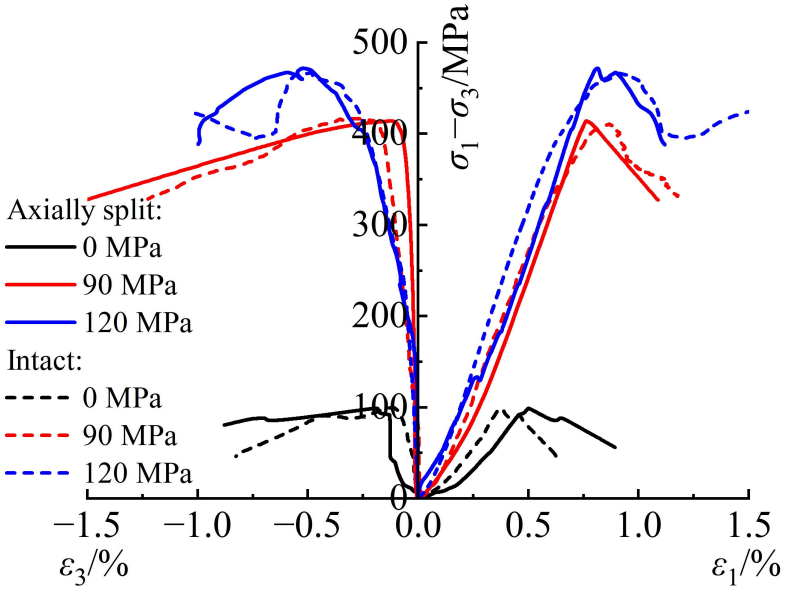


**Figure 4.** Comparison between intact specimens and axially split specimens.

Figure 5 is the uniaxial compression response of the axially cut specimen under different prefabricated fracture parameters. Figures 6 and 7 are the triaxial compression response under the confining pressure of 90 MPa and 120 MPa, respectively.

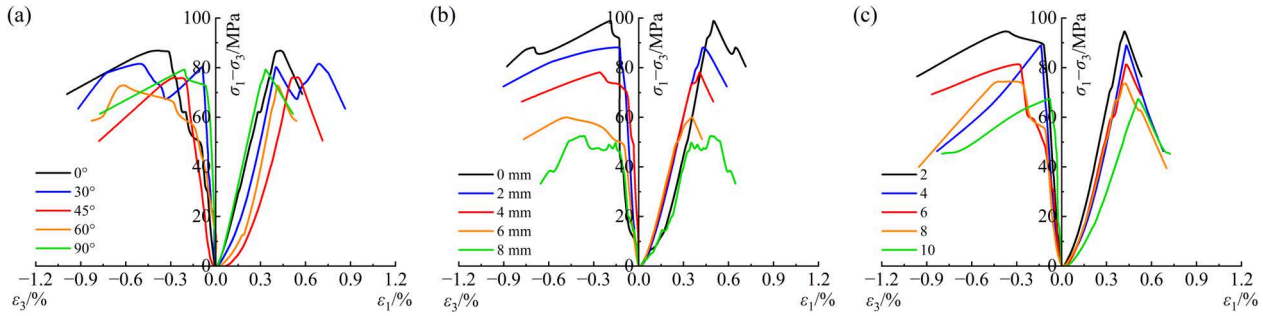


**Figure 5.** Stress–strain curves of different fracture parameters under uniaxial compression. (**a**) Different fracture angles; (**b**) different fracture widths; (**c**) different fracture densities.

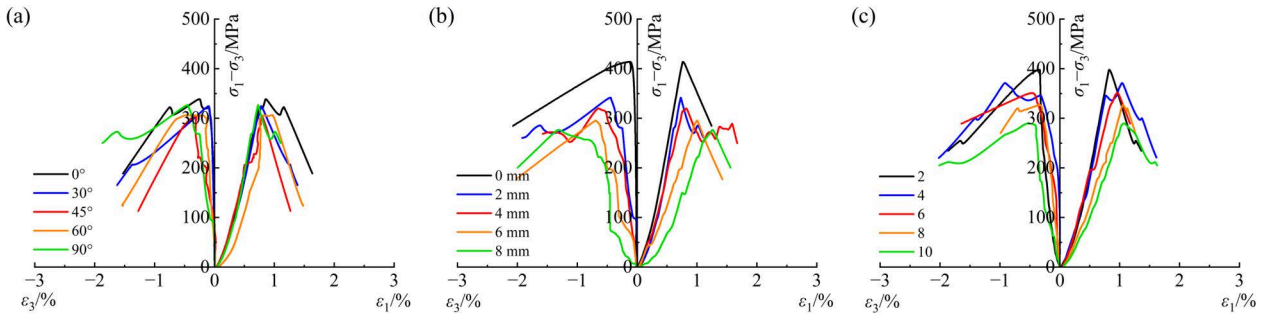


**Figure 6.** Triaxial compression experiments with different fracture conditions ($\sigma_3$ = 90 MPa). (**a**) Different fracture angles; (**b**) different fracture widths; (**c**) different fracture densities.

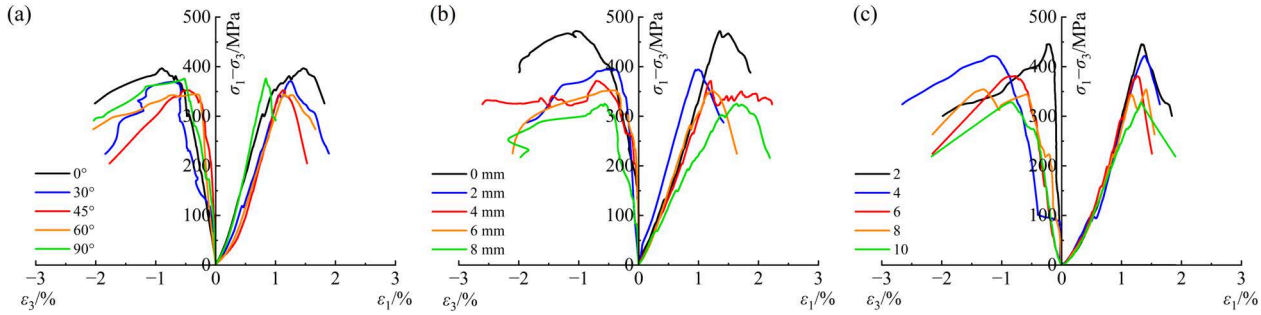


**Figure 7.** Triaxial compression experiments with different fracture conditions ($\sigma_3$ = 120 MPa). (**a**) Different fracture angles; (**b**) different fracture widths; (**c**) different fracture densities.

It can be seen from Figures 5a–7a that the fracture dip angle has a significant effect on the bearing capacity of rock specimens. Under both uniaxial and triaxial conditions, the peak strength decreases first and then rises with the increase in fracture inclination angle. The bearing capacity of specimens with 0° and 90° is stronger, and the strength near 45° is the lowest, indicating that the fractures with medium inclination angle are most prone to shear slip under compression load, which is a sensitive orientation to control the instability of rock specimens. When the confining pressure increases from 0 MPa to 90 MPa and 120 MPa, the peak strength and peak strain of the specimens with different dip angles are significantly improved, indicating that the confining pressure can inhibit the fracture opening and tip expansion, but it does not change the control effect of the dip angle on the strength ranking, and the brittle instability characteristics induced by fractures still exist.

As shown in Figures 5b–7b, increasing fracture width leads to a continuous decrease in the peak strength of the rock specimens, while enhancing pre-peak nonlinear deformation and compaction characteristics. Under uniaxial conditions, wider fractures are mainly manifested by a prolonged compaction stage and intensified post-peak softening. Under high confining pressure, fracture closure is constrained, and the specimens exhibit certain pre-peak fluctuation strengthening or progressive yielding characteristics; however, the load-bearing degradation caused by wide fractures does not disappear. This indicates that fracture width not only reflects the scale of the initial defects but also governs fracture closure, slip, and the space available for stress release. Confining pressure can only delay the instability process of specimens with wide fractures, but it is difficult to fully restore their load-bearing continuity.

It can be seen from Figures 5c–7c that the increase in fracture density generally reduces the peak strength of rock specimens and enhances the pre-peak nonlinear deformation. The low-density fracture specimen still retains a relatively complete matrix bearing skeleton, while the interaction between fractures in the high-density fracture specimen is enhanced, and it is easier to form a synergistic penetration failure. The increase in confining pressure

can improve the overall strength of the specimen and delay the fracture propagation. However, when the number of fractures is large, the fracture network effect gradually dominates, and the strength weakening is more obvious.

Based on the test results of uniaxial compression, confining pressure 90 MPa and confining pressure 120 MPa, it can be seen that the fracture geometric parameters and confining pressure form two competing control mechanisms on the mechanical behavior of rock specimens: the fracture parameters produce structural weakening effect, and the confining pressure produces constraint strengthening effect.

The fracture dip angle mainly determines whether the fracture is prone to shear activation, and the fracture with medium dip angle is the most unfavorable. The fracture width mainly controls the fracture closure, slip, and deformation release capacity. The larger the width, the weaker the bearing capacity. The fracture density mainly determines the degree of synergy between fractures. The higher the density, the easier the overall damage is formed. In contrast, the increase in confining pressure can significantly improve the peak strength and peak deformation capacity of the specimen, and delay the fracture propagation and damage penetration process, but it does not change the overall order of the influence of different fracture parameters on the strength.

Therefore, the fractured rock mass presents a response characteristic with engineering significance in the deep high confining pressure environment: the confining pressure can achieve 'strength recovery', but the fracture still retains the ability to control the failure path, that is, the strength is strengthened and the brittle memory does not disappear. For the deep fractured rock mass in Fuman Oilfield, the medium dip angle, large width, and high-density fractures are still the key structural factors to control the wellbore stability and the risk of surrounding rock instability. Although the high confining pressure improves the overall bearing capacity of the rock mass, once the fractures are synergistically activated, sudden failure may still be induced.

### *3.2. Evolution Law of Mechanical Parameters of Fractured Rock Mass*

Based on the stress–strain curves from Figures 5–7, the evolution law of Young's modulus and Poisson's ratio of fractured rock mass is calculated and analyzed. The Young's modulus and Poisson's ratio under each working condition were calculated using Equations (1) and (2), respectively, as shown in Figures 8 and 9.

Figure 8 shows the evolution law of Young's modulus of fractured rock mass. The change in Young's modulus in the figure can be mainly attributed to the coupling effect of fracture geometric characteristics and confining pressure. In general, after the confining pressure increases from 0 MPa to 90 MPa and 120 MPa, the Young's modulus of each group of specimens is significantly improved, indicating that the confining pressure can promote the fracture closure, weaken the deformation flexibility caused by the initial defects and enhance the deformation resistance of the rock skeleton. However, the increase in modulus under different fracture parameters is not consistent, indicating that the strengthening effect of confining pressure is controlled by the fracture structure, and it is not equivalent to the recovery of all fractured rock mass.

Under the condition of different dip angles (Figure 8a), the Young's modulus decreases first and then increases, with the lowest at 45° and the highest at 90°, indicating that the shear slip is most likely to occur in the middle dip angle fracture. The higher the confining pressure is, the more obvious the orientation difference is, which reflects the confining pressure strengthening effect of orientation selectivity. With the increase in fracture width and density (Figure 8b,c), the Young's modulus decreases generally, indicating that both wide fractures and dense fractures will enhance the structural softening, and the increase

in fracture density will also promote the synergistic deformation between defects, so that the stiffness recovery caused by confining pressure closed fractures is limited.

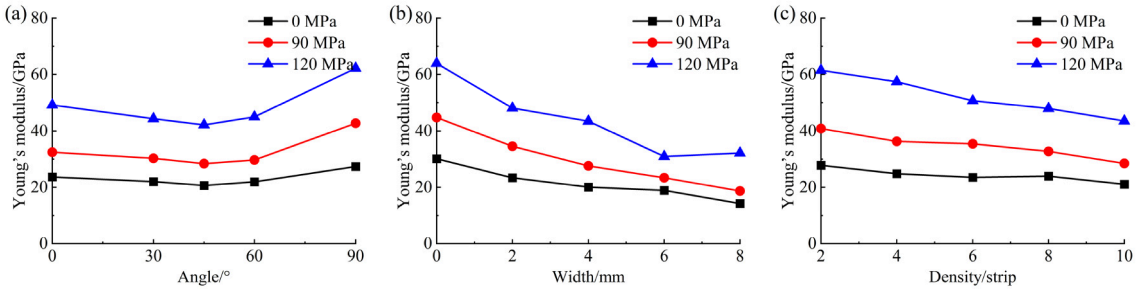


**Figure 8.** Evolution of Young's modulus with fracture parameters. (**a**) Different fracture angles; (**b**) different fracture widths; (**c**) different fracture densities.

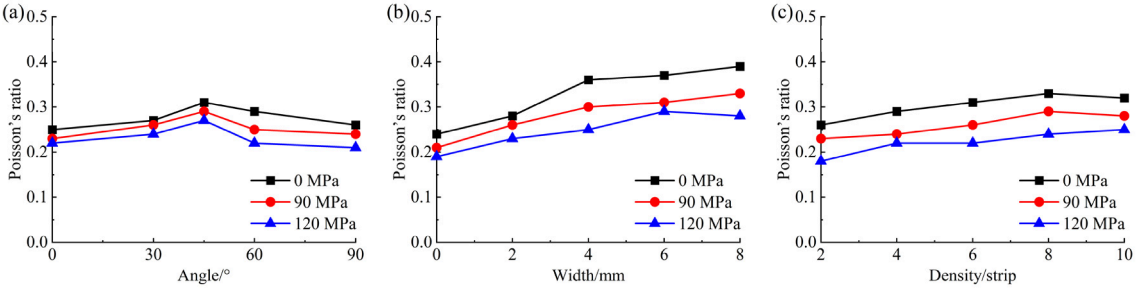


**Figure 9.** Evolution of Poisson's ratio with fracture parameters. (**a**) Different fracture angles; (**b**) different fracture widths; (**c**) different fracture densities.

The Young's modulus of rock specimens with fractures is controlled by the competition mechanism of 'fracture softening-confining pressure stiffening'. Confining pressure improves the overall stiffness by closing fractures and restraining deformation, while fracture dip angle, width and density control slip sensitivity, residual flexibility and synergistic damage degree, respectively. Therefore, although the deep high confining pressure environment can significantly improve the stiffness of rock mass, it cannot eliminate the structural deterioration effect caused by medium dip angle, wide fracture and high-density fracture.

Under the premise that the influence of axial splitting on the mechanical properties of the specimen datum can be ignored, the change of Poisson's ratio in the diagram mainly reflects the coupling effect of fracture structure and confining pressure. In general, Poisson's ratio decreases with the increase in confining pressure, indicating that confining pressure can effectively inhibit fracture opening, slip, and lateral expansion while improving strength and stiffness.

Under different dip angles (Figure 9a), the Poisson's ratio increases first and then decreases with the increase in the fracture angle, and the 45° specimen is the highest, indicating that the orientation is most likely to induce shear slip and lateral deformation of the fracture. After the confining pressure increases, the Poisson's ratio of each dip angle specimen decreases as a whole, but the deformation sensitivity of 45° remains. As the fracture width increases (Figure 9b), the Poisson's ratio generally increases, indicating that the wide fracture provides more space for closure dislocation and lateral deformation. Although high confining pressure can weaken this effect, it is difficult to completely eliminate the deformation deterioration caused by wide fractures. The increase in fracture density also leads to the overall increase in Poisson's ratio (Figure 9c), and the increase slows down or fluctuates slightly in the high-density interval, indicating that the fracture gradually changes from independent deformation to synergistic response under mutual constraints.

Combined with the results of peak strength and Young's modulus, it can be seen that the strength and stiffness of deep fractured rock mass recover with confining pressure, while the structural deformation sensitivity is still controlled by fractures. Among them, 45° fractures, larger width and higher density fractures are still the key unfavorable factors for lateral deformation and instability risk.

### *3.3. Strength Characteristics of Fractured Rock Mass*

This paper focuses on the strength response of fractured rock mass under deep high ground stress conditions. The equivalent Mohr–Coulomb envelope in the high confining pressure range is established by using the failure Mohr circle under the confining pressure of 90 MPa and 120 MPa. It can be seen from Figure 10 that there is a certain deviation between the uniaxial failure Mohr circle and the high confining pressure envelope, indicating that the fractured rock mass has different failure control mechanisms under low and high constraints. Therefore, in this paper, the obtained parameters are not regarded as the inherent strength parameters in the whole confining pressure range but are used to evaluate the influence of fracture dip angle on the shear bearing capacity of rock mass under high confining pressure. The comparison of envelope curves with different dip angles can further reveal the control effect of fracture conditions on the strength deterioration degree of high geo-stress rock mass.

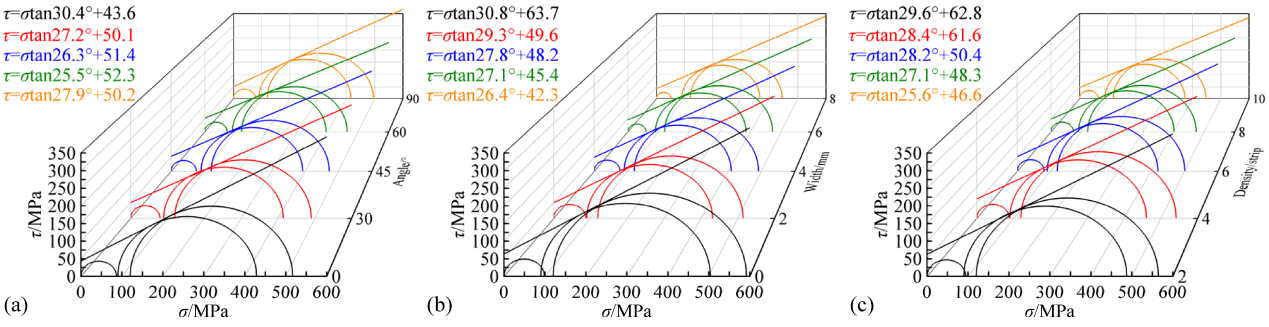


**Figure 10.** Strength envelopes under high in-situ stress conditions for different fracture configurations. (**a**) Different fracture angles; (**b**) different fracture widths; (**c**) different fracture densities.

Different fracture parameters have obvious influence on the shape of the envelope. The fracture angle mainly changes the slope of the envelope line, and the equivalent internal friction angle corresponding to the medium dip angle fracture is lower, indicating that it is still more prone to shear slip under high confining pressure, which is a sensitive orientation to control the instability of rock mass. As the fracture width increases, the strength envelope moves down as a whole, and the equivalent cohesion and internal friction angle decrease, indicating that the wide fracture weakens the interlocking bearing and friction impedance after the fracture is closed. The increase in fracture density also leads to the downward movement and slowing down of the envelope, reflecting the gradual transformation of fractures from isolated defects to collaborative failure of fracture network.

It can be seen from Figure 11a that with the increase in fracture angle, the internal friction angle decreases first and then rises, from about 30° at 0° to the lowest near 60°, and recovers at 90°. Cohesion increased first and then decreased slightly. It is shown that the fracture dip angle mainly controls the slip sensitivity of the fracture surface under high confining pressure, and the fracture with medium dip angle weakens the friction impedance, but the confining pressure closure effect will improve the contact occlusion and equivalent cohesion contribution of the fracture surface to a certain extent, which reflects the characteristics of 'friction weakening-closure compensation' under the control of orientation.

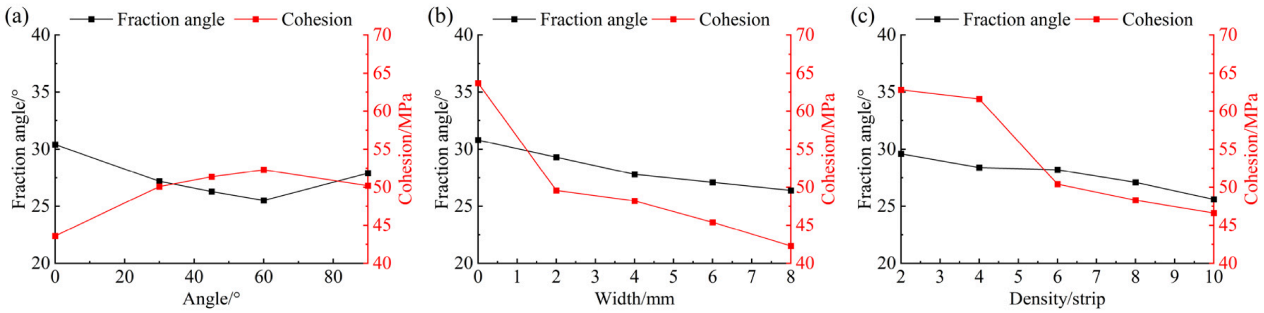


**Figure 11.** Evolution of cohesion and internal friction angle with fracture parameters. (**a**) Different fracture angles; (**b**) different fracture widths; (**c**) different fracture densities.

It can be seen from Figure 11b that as the fracture width increases from 0 mm to 8 mm, the internal friction angle and cohesion continue to decrease, indicating that the fracture width has a synchronous weakening effect on the strength parameters. The wide fractures are difficult to be completely closed even under high confining pressure, and the dislocation space and residual flexibility of the structural plane are large, thus reducing the friction interlocking ability and the overall cementation bearing capacity after closure. It can be seen from Figure 11c that the increase in fracture density also leads to the decrease in two types of parameters, in which the cohesion decreases more obviously between 4 and 6 fractures, indicating that after the number of fractures increases, the failure of rock specimens gradually changes from single fracture control to fracture network cooperative penetration control, and there is a certain structural deterioration mutation characteristics.

On the whole, the fracture angle mainly affects the friction slip mechanism, the fracture width controls the recovery degree of bearing continuity, and the fracture density determines the synergistic weakening level of the fracture group.

The sensitivities of the mechanical and strength parameters to the fracture parameters were calculated using Equation (3). The sensitivity of Young's modulus, Poisson's ratio, internal friction angle, and cohesion to fracture angle, width, and density is shown in Table 2.

**Table 2.** Sensitivity of mechanical parameters to fracture characteristics.

| Parameter | Confining Pressure Condition | $S_\alpha$ | $S_d$ | $S_\rho$ | Sensitivity Ranking |
|---|---|---|---|---|---|
| Young's Modulus | 0 MPa | 0.236 | 0.688 | 0.406 | $S_d > S_\rho > S_\alpha$ |
| | 90 MPa | 0.271 | 0.787 | 0.426 | $S_d > S_\rho > S_\alpha$ |
| | 120 MPa | 0.283 | 0.661 | 0.413 | $S_d > S_\rho > S_\alpha$ |
| Poisson's Ratio | 0 MPa | 0.356 | 0.534 | 0.443 | $S_d > S_\rho > S_\alpha$ |
| | 90 MPa | 0.310 | 0.490 | 0.349 | $S_d > S_\rho > S_\alpha$ |
| | 120 MPa | 0.305 | 0.492 | 0.346 | $S_d > S_\rho > S_\alpha$ |
| Cohesion | Comprehensive strength envelope | 0.105 | 0.369 | 0.363 | $S_d > S_\rho > S_\alpha$ |
| Friction Angle | Comprehensive strength envelope | 0.125 | 0.145 | 0.173 | $S_\rho > S_d > S_\alpha$ |

Note: $S_\alpha$ is the angle sensitive coefficient; $S_d$ is the sensitivity coefficient to fracture width; $S_\rho$ is the sensitivity coefficient to fracture density.

As shown in Table 2, the Young's modulus and Poisson's ratio are most sensitive to fracture width under uniaxial condition and confining pressures of 90 MPa and 120 MPa, followed by fracture density, while fracture angle has the weakest effect. Among different

fracture angles, those in the range of 30° to 60° exert the most significant influence on the Young's modulus and Poisson's ratio. In contrast, the sensitivity of cohesion to fracture width and density is relatively close, with values of 0.363 and 0.369, respectively, and the influence of fracture angle is minor. Fracture density has the greatest impact on the internal friction angle, followed by fracture width, and fracture angle has the weakest effect. Fracture angle mainly affects the variation path of strength parameters, while fracture width and density are the dominant factors controlling the degradation of shear strength parameters.

### *3.4. Failure Mode and Damage Characteristics of Fractured Rock Mass*

Figure 12 shows the failure modes of specimens with different fracture angles, widths and densities under uniaxial, 90 MPa and 120 MPa confining pressures. In general, the failure of fractured carbonate rocks is not simply controlled by confining pressure or fracture alone, but shows obvious coupling characteristics of 'confining pressure constraint strengthening-fracture path guidance control'. Under uniaxial conditions, the specimens are mainly axial tension splitting, the main fractures are relatively straight, and the failure path is induced by prefabricated fractures, but the whole is still relatively simple. After entering the high confining pressure condition, the fracture opening is inhibited, but the pre-peak energy storage capacity of the specimen is enhanced, the number of secondary fractures increases during failure, the fracture bifurcation, penetration, and local shear damage are more obvious, and the failure mode is gradually transformed from single tension to tension-shear composite failure.

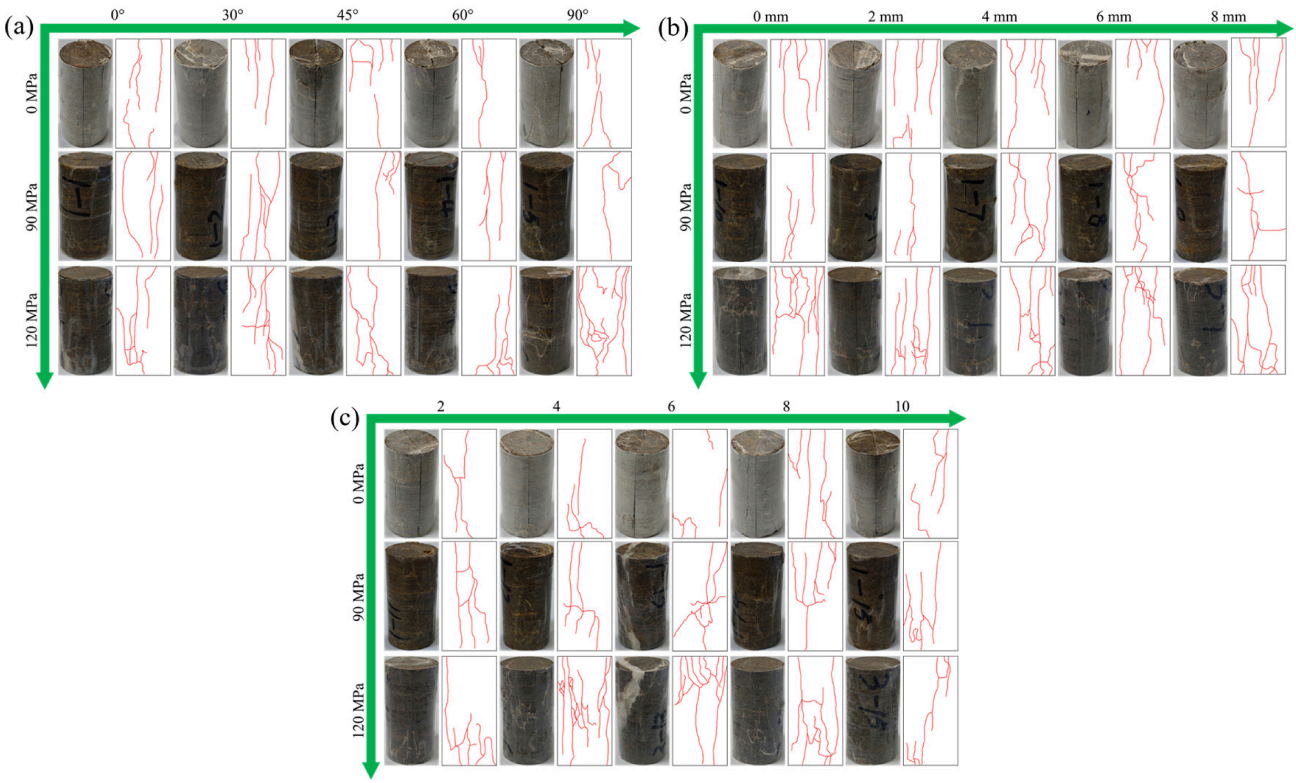


**Figure 12.** Failure modes of specimens under different fracture parameters and different confining pressures. (**a**) Different fracture angles; (**b**) different fracture widths; (**c**) different fracture densities.

It can be seen from Figure 12a that the failure paths of 0° and 90° specimens are relatively concentrated, which are mainly characterized by splitting along the axial direction or near the prefabricated fractures. The 30–60° oblique fractures are more easily activated

by shear, and the main fractures extend along the end of the prefabricated fractures and are accompanied by multi-stage bifurcation, indicating that the medium-angle fractures are sensitive structures that induce shear slip and local instability under high confining pressure. With the increase in confining pressure, the guiding and controlling effect of fracture angle on the failure path is not weakened, but it is more prominent in the development and fragmentation of shear fractures.

It can be seen from Figure 12b that the increase in width makes the failure of the specimen change from local splitting to multi-fracture synergistic expansion. The narrow fracture specimen still retains strong integrity, while the wide fracture is closed under high confining pressure, but the stress concentration and dislocation space at both ends are still obvious, resulting in dense development of secondary fractures and expansion of damage range. It shows that the wide fractures are not completely 'healed' under high confining pressure, but are transformed into weak structural planes that control shear dislocation and fracture re-expansion. It can be seen from Figure 12c that the increase in the number of fractures significantly increases the complexity of damage. The low-density specimen is controlled by a small number of main fractures, while the high-density specimen shows multi-fracture bifurcation, intersection, and penetration, and the failure is changed from single-fracture induction to fracture network synergistic control. Especially under the confining pressure of 120 MPa, the fracture network characteristics are more obvious, indicating that the high confining pressure improves the bearing capacity, and also makes the fracture group release stronger damage accumulation effect after the peak. It should be noted that, in Figure 12c, the specimen tested under a confining pressure of 120 MPa with a fracture density of 6 contains a vein-like natural heterogeneous structure, which is most likely a calcite vein or a locally mineral-filled body within the carbonate rock. Such natural heterogeneities may generate local stiffness contrasts and induce stress concentration, thereby altering subtle crack deflection, branching, and local coalescence paths. However, the overall failure mode of this specimen remains dominated by the interaction of multiple fractures and the coalescence of the fracture network, which is consistent with the general failure characteristics of high-fracture-density specimens under high confining pressure. Therefore, this local heterogeneous structure only modifies the local failure morphology and does not overturn the core conclusion: increasing fracture density intensifies the synergistic damage evolution of fractures and promotes the formation of connected failure in fractured carbonate rocks.

In general, high confining pressure can inhibit the early opening of fractures and improve the strength of specimens, but it cannot eliminate the control effect of fracture structure on the failure path. The fracture angle determines the direction of shear activation, the fracture width determines the dislocation ability of weak surface, and the fracture density determines the degree of damage network. It reveals the mechanical nature of deep fractured carbonate rocks that 'strength is strengthened and failure is guided by fractures' under high ground stress environment.

## 4. Stability Analysis of Fractured Reservoir

### *4.1. Construction of Fracture Damage Model*

In order to quantitatively characterize the deterioration law of mechanical parameters of carbonate rocks under the coupling of fracture geometric parameters and confining pressure, this paper regards fractured carbonate rocks as equivalent damage bodies. The fracture angle, width and density jointly control the damage degree of rock mass structure, while the increase in confining pressure will close the fracture and inhibit the fracture propagation. Therefore, the deterioration of mechanical parameters of fractured rock mass can be expressed as the result of the joint action of fracture damage effect and confining

pressure inhibition effect. The purpose of the damage model is to characterize, from the perspective of an equivalent continuum medium, the combined degradation effects of fracture inclination angle, fracture width, and fracture density on the macroscopic mechanical parameters of the rock.

Thus, the confining pressure-fracture coupling damage model is established:

$$D_P = \frac{a_P F_\alpha + b_P F_d + c_P F_\rho}{1 + k_P \frac{\sigma_3}{\sigma_{c0}}} \tag{4}$$

In the equation, $D_P$ is the damage variable of the mechanical parameter $P$; $F_\alpha$, $F_d$, and $F_\rho$ are the damage factors of fracture angle, width, and density, which are defined as $F_\alpha = \sin^2 2\alpha$, $F_d = d/d_{max}$, and $F_\rho = \rho/\rho_{max}$, respectively, where $\alpha$ is the fracture angle, $d$ is the fracture width and $\rho$ is the fracture density. $a_P$, $b_P$, and $c_P$ are the damage weights of the fracture angle, width, and density to the mechanical parameters, which are obtained by fitting the experimental data. $k_P$ is the confining pressure inhibition coefficient; $\sigma_3$ is confining pressure; $\sigma_{c0}$ is uniaxial compressive strength, which is used for dimensionless confining pressure.

Then the equivalent Young's modulus and cohesion of fractured carbonate rocks can be written as:

$$P^* = P_0(1 - D_\rho) \tag{5}$$

In the equation, $P^*$ is the equivalent mechanical parameter after damage; $P_0$ is the mechanical parameters of the complete specimen.

Poisson's ratio is corrected by increment:

$$v^* = v_0(1 + D_v) \tag{6}$$

In the equation, $v^*$ is the Poisson's ratio after considering damage; $v_0$ is the Poisson's ratio of the complete specimen.

For different mechanical parameters, the damage variables under different confining pressures and fracture conditions were determined using Equations (5) and (6). Subsequently, in combination with Equation (4), regression fitting was performed using the least-squares method, with the minimization of the residual sum of squares between the experimentally derived damage variables and the model-predicted damage variables taken as the objective function. The parameter values adopted in the damage model are presented in Table 3. To quantitatively evaluate the fitting accuracy of the model, the coefficient of determination, root mean square error, and mean absolute error were adopted as evaluation metrics. The coefficient of determination, root mean square error, and mean absolute error calculated from Table 3 indicate that the model exhibits relatively low prediction errors for damage.

**Table 3.** Damage model parameters.

| Parameter | $a_P$ | $b_P$ | $c_P$ | $k_P$ | Goodness of Fit |
|---|---|---|---|---|---|
| Young's modulus | 0.1539 | 0.5230 | 0.1543 | 0.1799 | 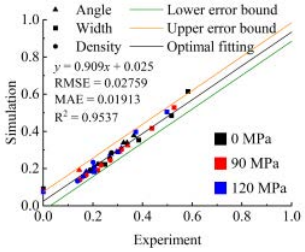 |

**Table 3.** *Cont.*

| Parameter | $a_P$ | $b_P$ | $c_P$ | $k_P$ | Goodness of Fit |
|---|---|---|---|---|---|
| Poisson's ratio | 0.0765 | 0.5997 | 0.1511 | 0.2455 | 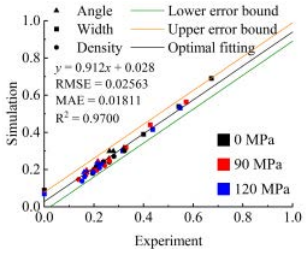 |



*4.2. Damage Model Calculation Verification*

The numerical model of triaxial compression is established based on Finite Difference Method, and the numerical simulation of triaxial compression under confining pressure of 90 MPa and 120 MPa is carried out, respectively. The numerical model is shown in Figure 13, and the simulation parameters of the complete specimen are shown in Table 4.

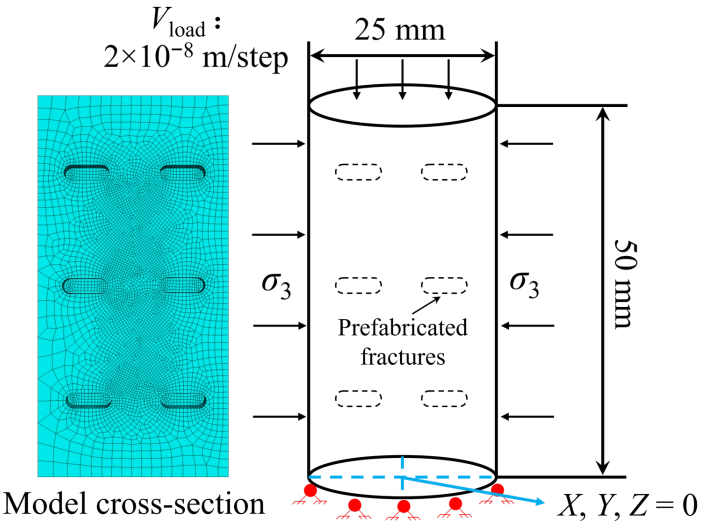


**Figure 13.** Numerical computational model.

**Table 4.** Parameters of intact specimens.

| Parameter | Young's Modulus/GPa | Poisson's Ratio | Cohesion/MPa | Friction Angle/° |
|---|---|---|---|---|
| Value | 30.13 | 0.24 | 63.7 | 30.3 |

The comparison of simulation and experimental results is shown in Figures 14 and 15. On the whole, the simulation curve is in good agreement with the experimental curve in the pre-peak loading section, peak strength, and axial strain evolution trend, which can accurately reproduce the elastic deformation, peak load, and post-peak instability characteristics of fractured rock specimens in the loading process, indicating that the established numerical model and damage model have good reliability.

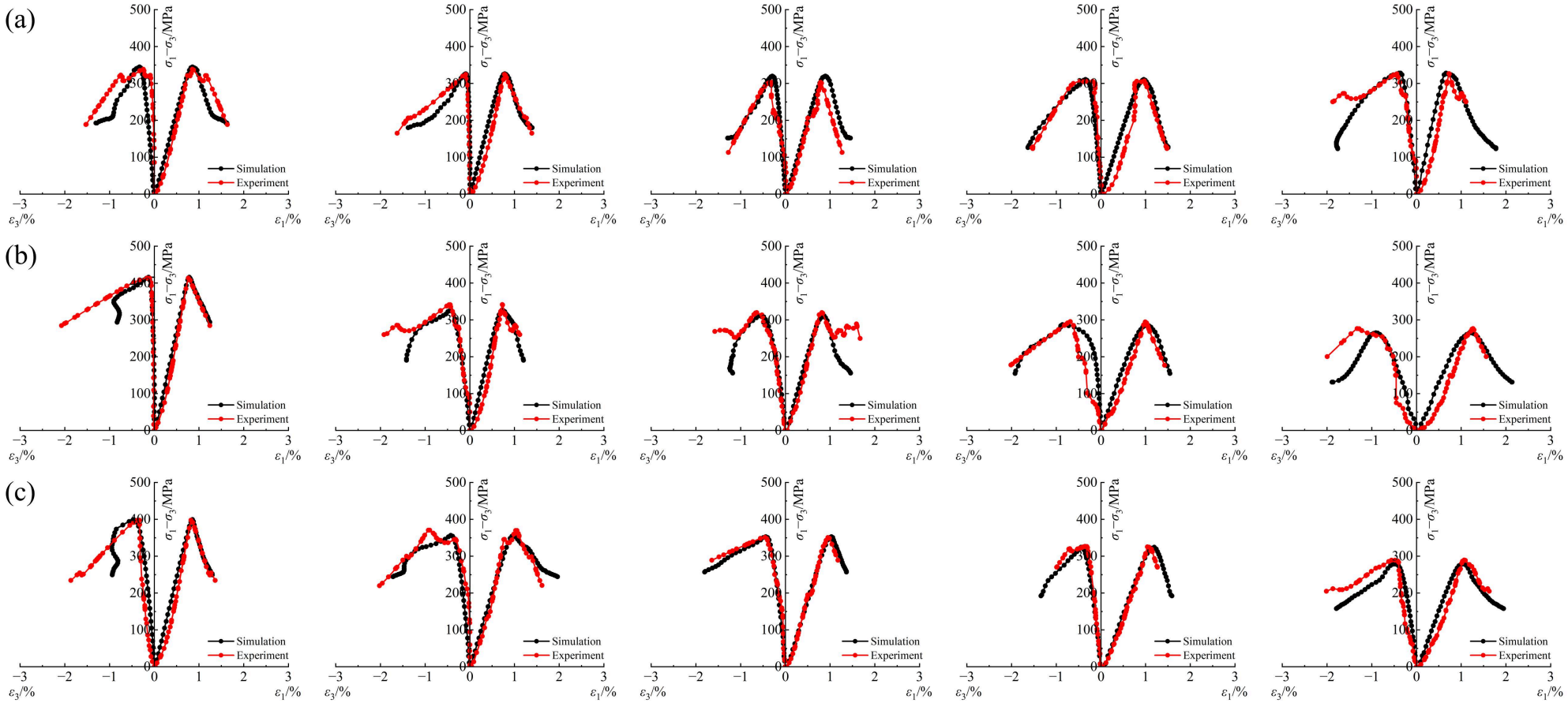


**Figure 14.** Comparison between simulated and experimental results at 90 MPa. (**a**) Different with fracture angles (0, 30, 45, 60, 90) (Unit: °); (**b**) different with fracture widths (0, 2, 4, 6, 8) (Unit: mm); (**c**) different with fracture densities (2, 4, 6, 8, 10) (Unit: strip).

https://doi.org/10.3390/pr14132108

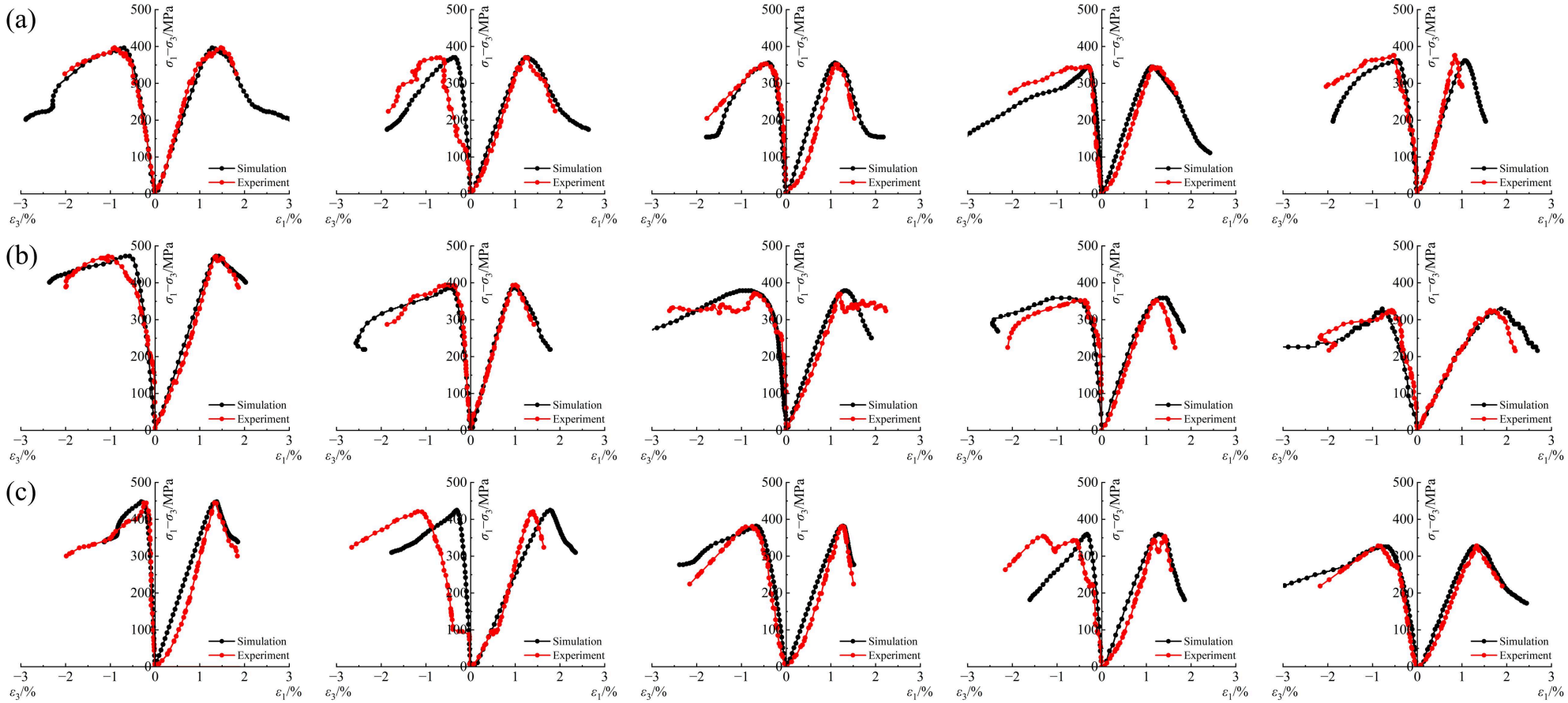


**Figure 15.** Comparison between simulated and experimental results at 120 MPa. (**a**) Different with fracture angles (0, 30, 45, 60, 90) (Unit: °); (**b**) different with fracture widths (0, 2, 4, 6, 8) (Unit: mm); (**c**) different with fracture densities (2, 4, 6, 8, 10) (Unit: strip).

https://doi.org/10.3390/pr14132108

However, some specimens have certain deviations in the post-peak stage and the radial strain side, and the experimental curve fluctuates significantly, while the simulation curve is relatively smooth. This is mainly related to the complex processes of natural carbonate rock heterogeneity, local fracture at the tip of the fracture, fracture closure and slip, and sudden penetration. In general, although the numerical model is difficult to completely reproduce the local random failure in the experiment, it can accurately grasp the main mechanical laws under the influence of fracture parameters. The comparison confirms that the damage model is reliable in simulating the strength degradation, deformation evolution, and instability mechanism of deep fractured rock mass.

After the predicted damage variables were calculated using the damage model, the predicted values of Young's modulus and Poisson's ratio were directly obtained from the model, whereas the peak strength was determined through triaxial compression numerical simulations based on the corrected mechanical parameters. The comparison between the model-predicted values and the experimental values is shown in Figure 16. The results indicate that the model can effectively capture the variation trends of the mechanical parameters of specimens under different fracture inclination angles, fracture widths, and fracture densities. Furthermore, the coefficient of determination, root mean square error, and mean absolute error show that the relative errors of peak strength, Young's modulus, and Poisson's ratio are generally within an acceptable range, indicating good agreement between the predicted and measured values, relatively small overall errors, and high predictive accuracy of the model.

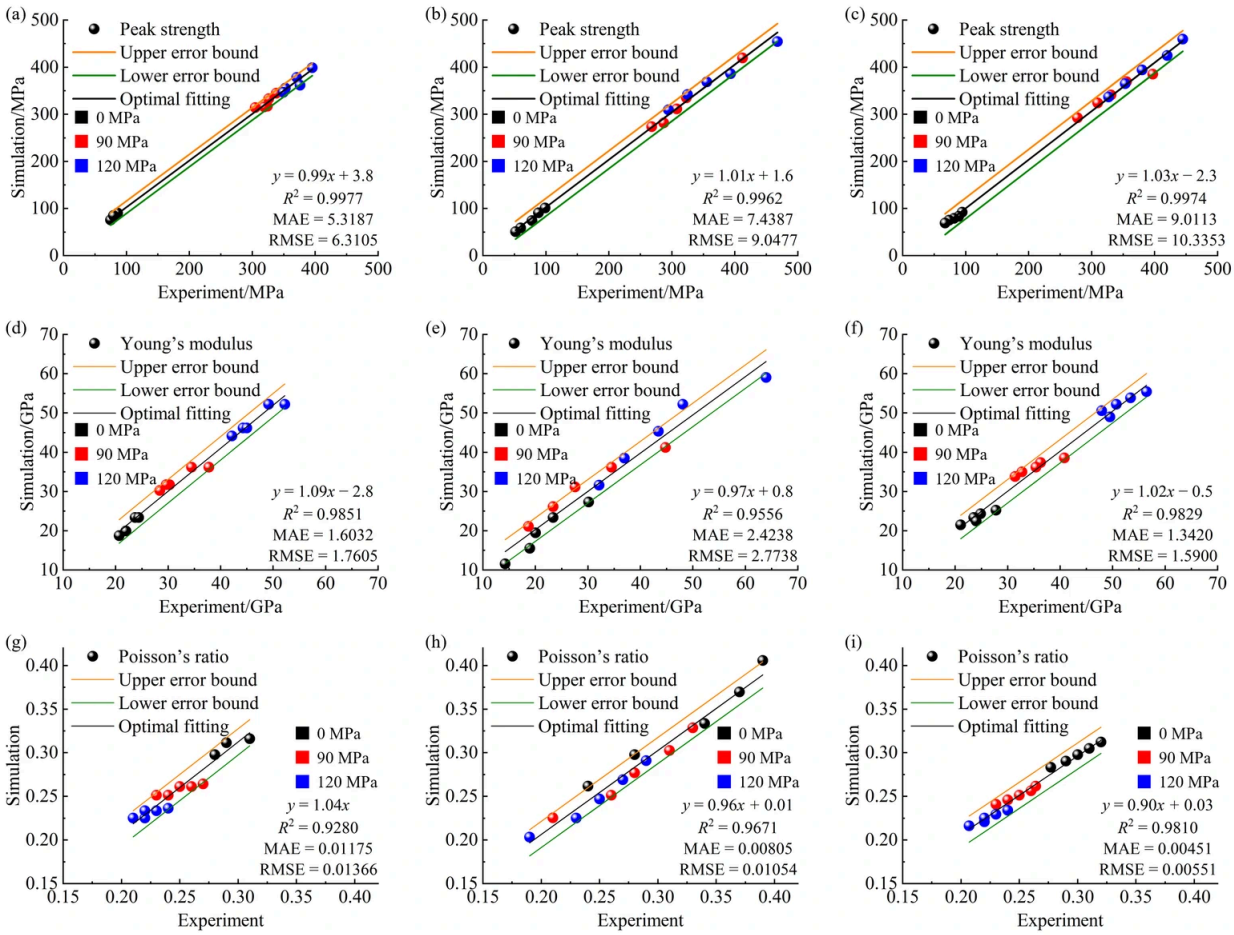


**Figure 16.** Error analysis between simulation and experimental results. (**a**) Error analysis of simulated and experimental peak strengths under different fracture angles; (**b**) error analysis of simulated and

experimental peak strengths under different fracture widths; (**c**) error analysis of simulated and experimental peak strengths under different fracture densities; (**d**) error analysis of simulated and experimental Young's modulus under different fracture angles; (**e**) error analysis of simulated and experimental Young's modulus under different fracture widths; (**f**) error analysis of simulated and experimental Young's modulus under different fracture densities; (**g**) error analysis of simulated and experimental Poisson's ratio under different fracture angles; (**h**) error analysis of simulated and experimental Poisson's ratio under different fracture widths; (**i**) error analysis of simulated and experimental Poisson's ratio under different fracture densities.

### *4.3. Simulation Results and Analysis*

Based on the damage theory model, the stability analysis model of ultra-deep reservoir is established. The model is shown in Figure 17. The length and width of the model are 3 m × 3 m, and only one cell is set in the axial direction of the well.

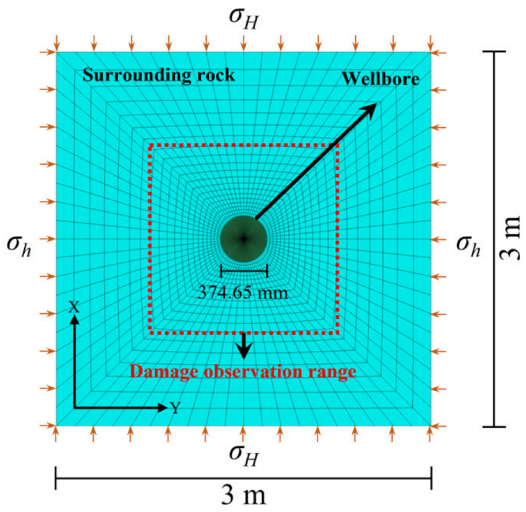


**Figure 17.** Wellbore stability analysis model.

The magnitude of the principal stress applied by the model is shown in Table 5. Since the model is a thin layer, it is set as a fixed boundary in the z direction, and the rock mass parameters used in the simulation are shown in Table 5. After the parameter assignment and the application of stress, the pre-calculation is carried out to reach the stress balance, and then the simulated excavation is carried out to remove the borehole part, and the simulation calculation of the stability of the fractured reservoir is carried out.

**Table 5.** In-situ stress conditions.

| In-Situ Stress Situation | Numerical Value/MPa |
|---|---|
| Maximum Horizontal Principal Stress $\sigma_H$ | 196.56 |
| Minimum Horizontal Principal Stress $\sigma_h$ | 134.57 |

Taking different fracture widths as examples, the stability simulation calculation of ultra-deep reservoir is carried out, and the simulation results are shown in Figure 18.

The simulation results indicate that damage does not propagate uniformly in the circumferential direction; rather, it is distinctly governed by the combined effects of horizontal in-situ stress anisotropy and fracture architecture. Circumferential compressive stress concentrations are more readily generated near the orientation of the minimum horizontal principal stress. Consequently, zones of severe damage predominantly extend toward the left and right sides, which is consistent with the established tendency for wellbore collapse to develop along the direction of the minimum horizontal principal stress.

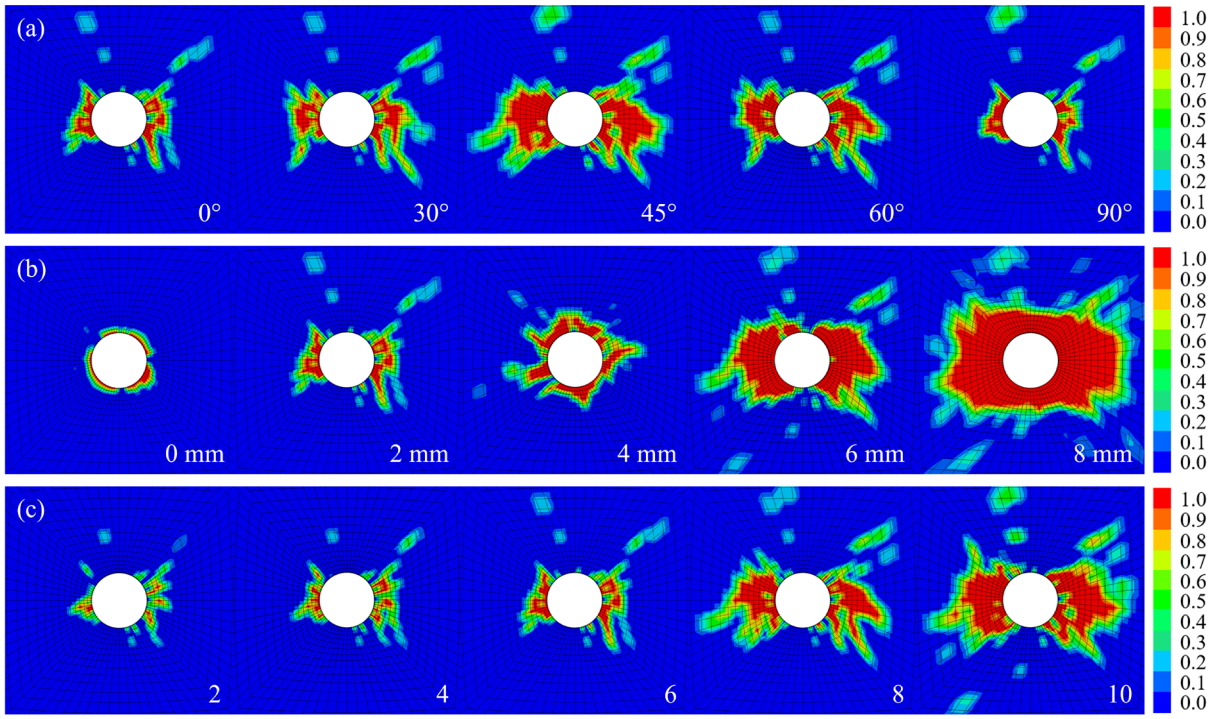


**Figure 18.** Wellbore stability analysis of reservoirs with different fracture parameters. (**a**) Fracture angles of 0°, 30°, 45°, 60°, and 90°; (**b**) fracture widths of 0 mm, 2 mm, 4 mm, 6 mm, and 8 mm; (**c**) fracture densities of 2, 4, 6, 8, and 10.

As shown in Figure 18a, at 0°, the high-damage zones are mainly distributed on the left and right sides of the wellbore, and the failure pattern is consistent with the lateral expansion characteristics controlled by the in-situ stress field, with fractures mainly exerting a local disturbance effect. As the fracture angle increases to 45°, the high-damage zones expand significantly. The superposition of wellbore stress concentration and fracture-tip stress concentration enhances the shear-slip effect of the fractures, causing damage to propagate rapidly into the surrounding rock. More continuous failure bands are formed on both sides of the wellbore, indicating that the coupling between fracture inclination and the in-situ stress direction is most pronounced at this angle. Under this condition, fractures transform from local defects into structural planes that guide damage propagation. When the angle increases to 90°, the damage pattern becomes more symmetrical again, and the outward propagation range decreases, suggesting that the inducing effect of vertical fractures on the lateral collapse zone is weakened.

As shown in Figure 18b, fracture width exerts a pronounced amplification effect on wellbore damage and exhibits a staged evolutionary pattern. At 0 mm, where no fracture is present, the high-damage zone is mainly distributed around the wellbore wall, while the surrounding rock remains largely intact, indicating that wellbore failure is primarily governed by stress concentration at the wellbore wall. At 2 mm, the high-damage zone remains confined to the near-wellbore region, with only a small number of discrete damage patches appearing. The fracture surfaces still retain a certain degree of closure and interlocking capacity, and their weakening effect on overall stability is limited. At 4 mm, damage begins to extend toward both sides of the wellbore, while fracture-tip stress concentration and local shear slip gradually participate in the failure process. The fractures thereby transform from weak disturbance factors into channels for damage propagation. At 6 mm, the damage zone expands significantly and forms a distinct banded failure region in the lateral direction, indicating that, with increasing fracture aperture, the constraining capacity of the fracture surfaces weakens and damage begins to propagate directionally

along the minimum horizontal principal stress direction. At 8 mm, high-damage zones develop continuously around the wellbore and form a large-scale connected failure band, demonstrating that large-aperture fractures have become the dominant structural planes controlling wellbore instability.

As shown in Figure 18c, fracture density primarily controls the degree of discreteness and connectivity of the damage zones. When the fracture density is 2, damage is mainly concentrated on both sides of the wellbore, with only a few isolated patches appearing in the surrounding rock. This indicates that, at low fracture density, no pronounced interaction has yet formed among the fractures, and wellbore failure is still dominated by single-fracture disturbance and stress concentration at the wellbore wall. When the density increases to 4, the high-damage zone around the wellbore becomes more pronounced and the number of peripheral damage spots increases, although the overall distribution remains discrete. At a density of 6, the damage zone extends further outward, and the stress disturbances at fracture tips begin to superimpose, indicating that the synergistic influence of the fracture group is gradually emerging. When the density reaches 8, relatively continuous lateral failure bands appear on both sides of the wellbore, suggesting that the damage zones induced by multiple fractures begin to connect and that the failure mode transitions from single-fracture control to fracture-group control. At a density of 10, the high-damage zones develop into large, connected regions, peripheral damage patches become more pronounced, and the overall integrity of the rock mass is significantly weakened.

Overall, Figure 18 demonstrates that the influence of fracture geometric parameters on wellbore stability exhibits a clear division of roles: medium-inclination fractures are most likely to induce shear slip and directional propagation, large-aperture fractures trigger threshold-type amplification of damage, and high-density fractures promote the evolution of discrete damage into a continuous failure network. Moreover, wellbore instability is not governed solely by in-situ stress concentration, but rather by the combined control of in-situ stress and fracture geometry. In-situ stress provides the driving force for failure, fracture angle determines the damage-release path, fracture width controls the degree of structural weakening, and fracture density determines whether damage can coalesce into a connected network. Under the influence of fractures, the evolution of wellbore damage presents a progressive instability mechanism characterized by "directional induction-strength amplification-network coalescence."

### *4.4. Engineering Implications and Limitations*

The experimental and numerical simulation results indicate that medium-inclination fractures, large-aperture fractures, and high-density fracture configurations are the most unfavorable to the mechanical stability of ultra-deep carbonate reservoirs. The development of such fractures reduces the equivalent strength and equivalent stiffness of the rock mass, causing wellbore failure to evolve gradually from localized and scattered damage to continuous through-going failure. Therefore, when evaluating wellbore stability in intervals with intense fracture development, the mechanical parameters of intact rock should not be used directly. Instead, rock-mass mechanical parameters corrected for fracture inclination angle, aperture, and density should be introduced for calculating collapse pressure and determining the safe drilling-fluid density window. The drilling-fluid density can be calculated using Equation (7):

$$\rho^* = \frac{P_c}{gH} \tag{7}$$

where, $\rho^*$ is the recommended drilling-fluid density; $P_c$ is the collapse stress, for which the corrected mechanical parameters should be used in fracture-developed intervals rather than the mechanical parameters of intact specimens; $g$ is the gravitational acceleration; and $H$ is

the true vertical depth. By using the corrected mechanical parameters in combination with the actual pore pressure and in-situ stress state, the drilling-fluid density can be optimized.

In addition, for unfavorable conditions such as medium-inclination fractures, large-width fractures, and high-density fractures, the optimization recommendations for drilling engineering are presented in Table 6.

**Table 6.** Drilling engineering optimization schemes under different fracture conditions.

| Fracture Condition | Instability Mechanism | Engineering Optimization Measures |
| --- | --- | --- |
| Medium fracture inclination angle | Shear slip is readily activated, and fracture-tip propagation is pronounced. | Optimize the wellbore azimuth and inclination to prevent dominant fracture sets from entering a highly shear-activated state; identify fracture occurrence using image logging; and calculate collapse pressure using the corrected strength parameters. |
| Large-width fractures | Fracture closure is incomplete, local slip space is large, and damage is prone to coalescence. | Increase the anti-collapse safety margin; enhance the plugging and bridging capacity of the drilling fluid; control fluid loss and pressure fluctuations; and adopt managed-pressure drilling when necessary. |
| High-density fractures | Fracture clusters undergo synergistic coalescence, leading to an expanded failure zone around the wellbore. | Shorten the open-hole interval; optimize the casing setting depth; and reduce swabbing and surge pressures during tripping operations. |
| Combined fractures with medium inclination angle, large-width, and high-density | Shear activation, weak-plane slip, and fracture-network coalescence act jointly. | Preferentially avoid intensely fractured intervals; design the drilling-fluid density window using fracture-corrected mechanical parameters; strengthen plugging and anti-collapse measures; and update the geomechanical model in real time. |

It should be noted that this study still has certain limitations. First, the laboratory tests were conducted on specimens containing prefabricated smooth fractures under controlled confining-pressure conditions, which differ from the fracture distribution characteristics in actual formations. Second, the occurrence environment of deep strata is highly complex, and factors such as high temperature, pore pressure, and water–rock chemical reactions should also be considered, as these factors may likewise alter fracture closure, shear slip, and damage accumulation in rocks.

In summary, the conclusions of this study can serve as a mechanical basis for rock-mass parameter correction and the evaluation of evolutionary trends. For practical field applications, further calibration and iterative refinement are required by integrating measured in-situ stress, pore pressure, formation fracture pressure, image logging data, and the specific geomechanical model of each individual well.

## 5. Conclusions

This study focuses on the Yingshan Formation carbonate rocks in the Fuman Oilfield of the Tarim Basin. Through laboratory uniaxial and triaxial compression tests, the effects of three fracture geometric parameters-fracture angle, width, and density on the stress–strain response, evolution of mechanical parameters, strength characteristics, and failure modes of the rock mass were systematically investigated under confining pressures of 0 MPa, 90 MPa, and 120 MPa. In addition, numerical simulations were conducted to analyze wellbore stability under different fracture conditions. Based on the experimental results of this study and the established confining pressure–fracture coupled damage model, practical support

can be provided for the engineering evaluation of ultra-deep fractured carbonate reservoirs. The model can correct the mechanical parameters of fractured carbonate rocks according to fracture inclination angle, fracture width, fracture density, and confining pressure, thereby supporting wellbore stability analysis, collapse pressure calculation, drilling-fluid density window design, and the identification of mechanically unfavorable fractured well intervals. The principal conclusions are as follows:

1. Fracture geometry and confining pressure jointly govern the mechanical properties of fractured carbonate rocks. Peak strength and Young's modulus first decrease and then increase with increasing fracture angle, with the most unfavorable condition occurring at approximately 45°. Increasing fracture width and density continuously weakens peak strength and Young's modulus while enhancing lateral deformation. High confining pressure improves the load-bearing capacity and suppresses lateral deformation, yet it cannot fully eliminate the degradation induced by fractures.
2. The sensitivity of mechanical parameters to fracture geometry varies significantly. Young's modulus and Poisson's ratio are most sensitive to fracture width, followed by fracture density, while fracture angle exerts the weakest influence. Among different fracture angles, the range of 30° to 60° has the most pronounced effect on mechanical parameters. Cohesion is primarily controlled by fracture width and density, whereas the internal friction angle is most sensitive to fracture density, indicating that densely distributed fractures are more likely to induce coordinated slip and shear instability.
3. Fractures and confining pressure jointly determine the failure modes and damage characteristics of fractured carbonate rocks. Under uniaxial compression, the rock mass is dominated by tensile splitting failure, whereas under high confining pressure, the failure mode evolves into a coupled tensile–shear failure. Fracture angle governs the direction of shear activation, fracture width controls weak-plane closure, slip, and the capacity for local damage propagation, while fracture density determines the degree of cooperative coalescence within fracture networks. Overall, the fractured rock mass exhibits the deep-rock mechanical characteristic that strength is enhanced by confining pressure, while failure is guided by fractures.
4. An equivalent mechanical-parameter correction method for fractured carbonate rocks was established based on normalized damage factors for fracture angle, width, and density, together with a confining-pressure suppression term. The wellbore stability simulations demonstrate that high in-situ stress controls the orientation of wellbore failure, fracture parameter governs the scale of damage propagation, and their coupled effect ultimately determines the wellbore stability of ultra-deep fractured carbonate reservoirs.

It should be noted that the experimental results and damage model in this study are based on specimens containing regular, relatively homogeneous, and smooth prefabricated fractures. The primary objective is to reveal, under controlled conditions, the effects of fracture inclination angle, width, and density on the mechanical properties of ultra-deep carbonate rocks, and to identify the basic influence trends of fracture geometric parameters on rock mechanical degradation and wellbore stability. Compared with natural fractures in actual reservoirs, further investigation is still required to analyze the shear strength, closure characteristics, and damage evolution of fractures with different roughness levels and infilling states under high confining pressure.

**Author Contributions:** Methodology, Z.W.; Software, X.W. and X.Z.; Validation, X.Z. and Y.D.; Formal analysis, H.Z. (Haoyang Zan); Investigation, C.M.; Resources, H.Z. (Hui Zhang); Data curation, Z.L. and W.Z.; Writing—original draft, Z.W. and X.Z.; Writing—review and editing, W.Y.; Supervision, W.Y.; Funding acquisition, W.Y. All authors have read and agreed to the published version of the manuscript.

**Funding:** This research received no external funding.

**Data Availability Statement:** The original contributions presented in this study are included in the article. Further inquiries can be directed to the corresponding authors.

**Conflicts of Interest:** Authors Zhimin Wang, Hui Zhang, Haoyang Zan, Xin Wang, Ziwei Liu, and Wentao Zhang were employed by PetroChina Tarim Oilfield Company, Korla and China National Petroleum Corporation. The remaining authors declare that the research was conducted in the absence of any commercial or financial relationships that could be construed as potential conflicts of interest.

## References

1. Zhu, G.Y.; Zhang, Z.Y.; Jiang, H.; Yan, L.; Chen, W.Y.; Li, T.T.; Li, X. Evolution of the Cryogenian cratonic basins in China, paleo-oceanic environment and hydrocarbon generation mechanism of ancient source rocks, and exploration potential in 10,000 m-deep strata. *Earth-Sci. Rev.* **2023**, *244*, 104506. [CrossRef]
2. Wang, Z.M.; Xu, K.; Zhang, H.; Wang, H.Y.; Yin, G.Q.; Wang, Z.H.; Zhao, W. Fracture effectiveness evaluation of ultra-deep tight sandstone reservoirs: A case study of the Keshen gas field, Tarim Basin, West China. *Front. Earth Sci.* **2022**, *10*, 883479. [CrossRef]
3. Xiong, R.; Fu, H.; Li, Y.; Xie, C.Z.; Wang, R.G.; Xiao, C.Y. Sequence and karst characteristics of the Middle-Lower Ordovician Yingshan Formation in Shuntuoguole area, Tarim Basin. *Deep Earth Energy Sci. Tech.* **2026**, *2*, 38–49. [CrossRef]
4. Cao, P.; Liu, T.Y.; Pu, C.Z.; Lin, H. Crack propagation and coalescence of brittle rock-like specimens with pre-existing cracks in compression. *Eng. Geol.* **2015**, *187*, 113–121. [CrossRef]
5. Ma, Z.; Pu, H.; Xue, K.S.; Hao, Z.; Liu, X.Y.; Qu, G.B.; Liu, D.J.; Yi, Q.Y. Bearing stability assessment of flawed sandstone considering multi-parameter coupling and analytic hierarchy process: Effects of flaw geometric configuration. *Theor. Appl. Fract. Mech.* **2026**, *143*, 105454. [CrossRef]
6. Cao, R.H.; Yao, R.B.; Meng, J.J.; Lin, Q.B.; Lin, H.; Li, S. Failure mechanism of non-persistent jointed rock-like specimens under uniaxial loading: Laboratory testing. *Int. J. Rock Mech. Min. Sci.* **2020**, *132*, 104341. [CrossRef]
7. Chen, N.; Xu, K.W.; Li, M.; Jia, B.Y.; Luo, Z.X. Study on the mechanical properties and fracture mechanism of granite with different rock bridge angles after ultra-low temperature treatment. *Eng. Fract. Mech.* **2026**, *341*, 112223. [CrossRef]
8. Liu, D.J.; Pu, H.; Xu, X.D.; Fan, Y.H.; Xue, K.S.; Liu, L.L.; Zhang, H.; Yi, Q.Y. Coupled effects of brittleness and fracture geometry on the damage evolution and mechanical degradation of sandstone. *Theor. Appl. Fract. Mech.* **2026**, *143*, 105480. [CrossRef]
9. Chen, Y.F.; Sheng, B.Y.; Xie, S.J.; Cao, R.H.; Wang, Y.X.; Zhao, Y.L.; Lin, H. Crack propagation and scale effect of random fractured rock under compression-shear loading. *J. Mater. Res. Technol.* **2023**, *23*, 5164–5180. [CrossRef]
10. Bai, Y.; Xu, Z.B.; Dou, H.Y.; Liu, N.Z.; Zhao, Z.Y.; Qiu, S.H.; Shan, R.L. Study on mechanical properties and mesoscopic damage mechanism of composite jointed rock masses. *Int. J. Min. Sci. Technol.* **2025**, *35*, 1731–1751. [CrossRef]
11. Chen, Y.F.; Lin, H.; Liang, L.Y. Freeze-thaw failure characteristics and strength loss of non-penetrating fractured rock mass with different fracture densities. *Theor. Appl. Fract. Mech.* **2023**, *124*, 103792. [CrossRef]
12. Zhou, C.T.; Rui, Y.C.; Qiu, J.D.; Wang, Z.H.; Zhou, T.; Long, X.T.; Shan, K. The role of fracture in dynamic tensile responses of fractured rock mass: Insight from a particle-based model. *Int. J. Coal Sci. Technol.* **2025**, *12*, 39. [CrossRef]
13. Jia, B.X.; Liu, F.P. Stress distribution characteristics and crack propagation law of fractured hard rock influenced by opening degree. *Geomech. Geophys. Geo-Energy Geo-Resour.* **2025**, *11*, 59. [CrossRef]
14. Li, X.D.; He, C.; Xu, G.W.; Chen, Z.W.; Ying, P.; Wu, J.; Jiang, Y. Model testing of fragmentation and fracture energy dissipation under rock blasting with various borehole diameters. *Eng. Fract. Mech.* **2026**, *343*, 112287. [CrossRef]
15. Yu, Y.; Li, J.Q.; Xia, Z.G. Porosity evolution and damage mechanism of fractured rock under drop hammer impact load. *Eng. Fail. Anal.* **2026**, *192*, 110844. [CrossRef]
16. Qin, C.A.; Wang, W.; Wang, J.; Chang, Y.W.; Pei, B.C.; Zhang, Y. Influence of bedding inclination and density on the fracture behavior of layered rock bridges under cyclic loading. *Theor. Appl. Fract. Mech.* **2026**, *145*, 105620. [CrossRef]
17. Li, K.S.; Chen, L.X.; Zhao, Z.; Liu, C.X. Experimental investigation on mechanical, acoustic, and fracture behaviors and the energy evolution of sandstone containing non-penetrating horizontal fissures. *Theor. Appl. Fract. Mech.* **2023**, *123*, 103703. [CrossRef]
18. Laghaei, M.; Baghbanan, A.; Hashemolhosseini, H.; Dehghanipoodeh, M. Numerical determination of deformability and strength of 3D fractured rock mass. *Int. J. Rock Mech. Min. Sci.* **2018**, *110*, 246–256. [CrossRef]

19. Hao, Y.M.; Wei, X.D.; Zhao, G.F. A comparison study on the predictive ability of numerical methods for fracturing of rock with different pre-existing flaws. *Int. J. Rock Mech. Min. Sci.* **2023**, *171*, 105584. [CrossRef]
20. Jarra, M.; Blocher, M.; Kluge, C.; Hollander, H.M. Elastic–plastic fracture propagation modeling in rock fracturing via punch through shear test. *Rock Mech. Rock Eng.* **2021**, *54*, 3135–3147. [CrossRef]
21. Hu, J.; Wang, H.K.; Xia, Z.G.; Chen, B.; Gu, Q.H.; Wang, X.R.; Cao, J.P.; Liu, X. Mechanical properties and acoustic emission characteristics of two dissimilar layers of rock-like specimens with prefabricated parallel fissures. *Geomech. Geophys. Geo-Energy Geo-Resour.* **2024**, *10*, 19. [CrossRef]
22. Zhu, Y.G.; Wu, Y.; Han, C.H.; Qiao, W.G.; Jiang, F.; Dong, J.X.; Zhang, S.; Li, Y.Z. Fracture evolution and anchoring mechanisms in discontinuous rock masses with irregular joints: Discrete element study using a novel damage constitutive model. *Comput. Geotech.* **2025**, *186*, 107395. [CrossRef]
23. Wang, R.J.; Li, Z.Y.; Dai, Y.H.; Li, J. Study on three-dimensional characterization of parameters and fracture opening and closing mechanism of ultra-deep carbonate reservoirs. *Deep Earth Energy Sci. Tech.* **2026**, *2*, 57–68. [CrossRef]
24. Xie, H.P.; Li, C.; He, Z.Q.; Li, C.B.; Lu, Y.Q.; Zhang, R.; Gao, M.Z.; Gao, F. Experimental study on rock mechanical behavior retaining the in situ geological conditions at different depths. *Int. J. Rock Mech. Min. Sci.* **2021**, *138*, 104548. [CrossRef]
25. Xia, Y.L.; Xu, D.P.; Qiu, S.L.; Liu, X.Y.; Huang, X.; Li, Z.G. Experimental Study on mechanical properties of deeply buried granite during layered excavation of large underground caverns. *Rock Mech. Rock Eng.* **2023**, *56*, 4757–4778. [CrossRef]
26. Wang, J.; He, M.M.; Wang, H.T.; Dang, F.N. Ductile-brittle failure transition of rocks subjected to temperature heating and water cooling in process of drilling with high confining pressure. *J. Appl. Geophys.* **2026**, *245*, 106037. [CrossRef]
27. Meng, Q.B.; Liu, J.F.; Xie, L.X.; Pu, H.; Yang, Y.G.; Huang, B.X.; Qian, W. Experimental mechanical strength and deformation characteristics of deep damaged–fractured rock. *Bull. Eng. Geol. Environ.* **2022**, *81*, 32. [CrossRef]
28. Wei, G.Q.; Zhao, Z.; Zhang, R.H.; Zhang, K.X.; Laubach, S.E.; Jia, C.Z.; Zeng, Q.L.; Yu, C.F.; Lai, J.; Xin, X.F. Fracture-pore networks and brittle with ductile stress-strain mechanisms: Triaxial tests on >7,600 m samples yield insights for 10,000 m deep sandstones. *Sci. China Earth Sci.* **2026**, *69*, 702–720. [CrossRef]
29. Zhou, Y.Q.; Sheng, Q.; Li, N.N.; Fu, X.D. The dynamic mechanical properties of a hard rock under true triaxial damage-controlled dynamic cyclic loading with different loading rates: A case study. *Rock Mech. Rock Eng.* **2022**, *55*, 2471–2492. [CrossRef]
30. Xia, Y.J.; Wang, Y.S.; Yang, H.; Zhao, D.C.; Yin, Z.Y.; Tang, C.A.; Chen, J. Studies on mechanical properties and failure characteristics of anisotropic shale under true triaxial loading at real-time high temperature. *Rock Mech. Rock Eng.* **2025**, *58*, 7203–7234. [CrossRef]
31. Liu, Z.B.; Wang, H.Y.; Li, Y.P.; Wang, X.; Selvadurai, A.P.S. Triaxial compressive strength, failure, and rockburst potential of granite under high-stress and ground-temperature coupled conditions. *Rock Mech. Rock Eng.* **2023**, *56*, 911–932. [CrossRef]
32. Yan, Z.W.; Zhang, R.; Zhang, Z.L.; Zhang, Z.T.; Xie, J.; Zhang, A.L.; Xiao, K. Quantitative analysis of surrounding rock response considering the dynamic coupling evolution of 3D strength criterion parameters and seepage parameters. *Tunn. Undergr. Space Technol.* **2026**, *174*, 107714. [CrossRef]
33. Li, K.T.; Zhu, L.; Xiong, F.; Liu, J.; Xue, Y.; Cao, Z.Z.; Zhou, Y.J.; Liang, X.; Ji, M.; Liu, G.N.; et al. Review on Thermal stimulation in deep geothermal reservoirs: Thermo-mechanical mechanisms and fracture evolution. *Processes* **2026**, *14*, 1199. [CrossRef]
34. Zhu, D.M.; Li, Y.N.; Huang, W.C.; Hu, X.W. Experimental study on physico-mechanical responses and energy characteristics of granite under high temperature and hydro-mechanical coupling. *Case Stud. Therm. Eng.* **2024**, *63*, 105245. [CrossRef]
35. Zhang, J.Z.; Long, Y.D.; Zhang, T.; Zhou, X.P. A true triaxial experiment investigation of the mechanical and deformation failure behaviors of flawed granite after exposure to high-temperature treatment. *Eng. Fract. Mech.* **2024**, *306*, 110273. [CrossRef]
36. Xue, Y.; Wang, L.C.; Cai, Y.H.; Liu, J.; Ranjith, P.G.; Gao, F.; Xie, H.P.; Liu, Y. Effects of heating–cooling on the mechanical properties and damage evolution of granite for underground cryogenic storage. In *Acta Geotechnica*; Springer: Berlin/Heidelberg, Germany, 2026. [CrossRef]
37. Ma, X.; Wang, G.L.; Hu, D.W.; Liu, Y.G.; Zhou, H.; Liu, F. Mechanical properties of granite under real-time high temperature and three-dimensional stress. *Int. J. Rock Mech. Min. Sci.* **2020**, *136*, 104521. [CrossRef]
38. Zhou, H.Y.; Liu, Z.B.; Shen, W.Q.; Feng, T.; Zhang, G.Z. Mechanical property and thermal degradation mechanism of granite in thermal-mechanical coupled triaxial compression. *Int. J. Rock Mech. Min. Sci.* **2022**, *160*, 105270. [CrossRef]
39. Ma, Y.S.; Cai, X.Y.; Yun, L.; Li, Z.J.; Li, H.L.; Deng, S.; Zhao, P.R. Practice and theoretical and technical progress in exploration and development of Shunbei ultra-deep carbonate oil and gas field, Tarim Basin, NW China. *Pet. Explor. Dev.* **2022**, *49*, 1–20. [CrossRef]
40. Li, C.; Pan, S.X.; Wang, H.B.; Deng, J.X.; Zhao, J.G.; Li, Z.; Zhang, Y. Rock physical characteristics of deep dolomite under complex geological conditions: A case study of 4th member of Sinian Dengying Formation in the Sichuan Basin, China. *Pet. Sci.* **2024**, *21*, 2370–2382. [CrossRef]
41. Du, H.; Xing, H.L.; Feng, J.W.; Xu, S.Y. Damage-integrated fracture prediction model for multi-stage fracture in deep carbonates: Application to the A Oilfield, Northern Tarim Basin. *Mar. Pet. Geol.* **2025**, *182*, 107599. [CrossRef]
42. Zhou, Q.; Zhu, Z.M.; Zhang, R.; Fan, Z.D.; Nie, X.F.; Gao, W.T.; Li, C.B.; Wang, J.; Li, R. Rock fracture initiation under deep extreme in situ conditions: A review. *J. Rock Mech. Geotech. Eng.* **2024**, *16*, 5297–5324. [CrossRef]

43. Wang, T.; Ye, W.W.; Liu, L.Y.; Liu, K.; Jiang, N.S.; Feng, X.H. Disturbance failure mechanism of highly stressed rock in deep excavation: Current status and prospects. *Int. J. Miner. Metall. Mater.* **2024**, *31*, 611–627. [CrossRef]
44. Waqar, M.F.; Qi, S.W.; Zheng, B.W.; Guo, S.F. Dynamic testing methods and failure properties of rocks: A comprehensive review. In *Rock Mechanics and Rock Engineering*; Springer: Berlin/Heidelberg, Germany, 2025. [CrossRef]
45. An, H.M.; Mu, X.H. Contributions to rock fracture induced by high ground stress in deep mining: A review. *Rock Mech. Rock Eng.* **2025**, *58*, 463–511. [CrossRef]
46. Ma, Z.Y.; Tao, S.; Yang, F.; Cui, Y.; Jing, Q.H.; Zhang, J.L.; Yan, S.Q.; Yu, B.; Guo, J.; Yang, D.; et al. Current status and development trends of deep rock mechanical properties: Experiments and simulations. In *Archives of Computational Methods in Engineering*; Springer: Berlin/Heidelberg, Germany, 2026. [CrossRef]
47. Zhao, G.K.; Guo, Y.T.; Yang, C.H.; Wang, L.; Guo, W.H.; Yang, H.Z.; Wu, X.L.; Liu, H.J. Anisotropic mechanical behavior of ultra-deep shale under high in-situ stress, a case study in the Luzhou block of the southern Sichuan Basin, China. *Int. J. Rock Mech. Min. Sci.* **2023**, *170*, 105536. [CrossRef]
48. Li, P.Y.; Liu, X.R.; Guo, X.Y.; Luo, X.Y.; Wang, G. Mechanical properties and failure mechanism of limestone containing notches subjected to uniaxial compression: An experimental and numerical study. *Theor. Appl. Fract. Mech.* **2026**, *141*, 105266. [CrossRef]
49. Wang, Y.L.; Tang, J.X.; Dai, Z.Y.; Ting, Y. Experimental study on mechanical properties and failure modes of low-strength rock samples containing different fissures under uniaxial compression. *Eng. Fract. Mech.* **2018**, *197*, 1–20. [CrossRef]
50. Wu, S.Y.; Huang, Y.H. Macro and meso crack evolution of granite specimens with non-straight fissures: A comparison between two bond models. *Theor. Appl. Fract. Mech.* **2023**, *125*, 103890. [CrossRef]
51. Li, P.; Cai, M.F.; Wang, P.T.; Guo, Q.F.; Miao, S.J.; Ren, F.H. Mechanical properties and energy evolution of jointed rock specimens containing an opening under uniaxial loading. *Int. J. Miner. Metall. Mater.* **2021**, *28*, 1875–1886. [CrossRef]
52. Chen, M.; Zang, C.W.; Ding, Z.W.; Zhou, G.L.; Jiang, B.Y.; Zhang, G.C.; Zhang, C.P. Effects of confining pressure on deformation failure behavior of jointed rock. *J. Cent. South Univ.* **2022**, *29*, 1305–1319. [CrossRef]
53. Davy, P.; Darcel, C.; Goc, R.L.; Ivars, D.M. Elastic properties of fractured rock masses with frictional properties and power law fracture size distributions. *J. Geophys. Res. Solid Earth* **2018**, *123*, 6521–6539. [CrossRef]
54. Wu, F.Q.; Deng, Y.; Wu, J.; Li, B.; Sha, P.; Guan, S.G.; Zhang, K.; He, K.Q.; Liu, H.D.; Qiu, S.H. Stress–strain relationship in elastic stage of fractured rock mass. *Eng. Geol.* **2020**, *268*, 105498. [CrossRef]
55. Yan, B.Q.; Kang, H.P.; Li, X.S.; Qi, Q.J.; Zhang, B.; Liu, J.Z. Damage constitutive model and mechanical properties of jointed rock mass under hydro-mechanical coupling. *Theor. Appl. Fract. Mech.* **2023**, *123*, 103735. [CrossRef]
56. Zheng, Z.; Li, R.H.; Zhang, Q. A novel anisotropic deterioration mechanical model for rock ductile–brittle failure under 3D high-stress and its application. *Comput. Geotech.* **2023**, *162*, 105665. [CrossRef]
57. Hu, J.Y.; Sheng, D.F.; Qin, F.F.; Zhu, Y.C.; Li, Z.H.; Chen, T.C.; Yu, H.Q. Progressive failure characteristics and damage constitutive model of fissured rocks under water–rock coupling. *Theor. Appl. Fract. Mech.* **2025**, *135*, 104765. [CrossRef]
58. Zhang, W.B.; Wang, G.W.; Cao, Z.C. Reactive Transport Modeling of Reflux Dolomitization of Carbonate Platforms: Enlightenment from Yingshan Formation in Shunnan Area, Tarim Basin. *Minerals* **2021**, *11*, 1340. [CrossRef]
59. *GB/T 50266-2013*; Standard for Test Methods of Engineering Rock Mass. China Planning Press: Beijing, China, 2013.